Alma Mater Studiorum – Università di Bologna

DOTTORATO DI RICERCA IN

SCIENZE BIOMEDICHE E NEUROMOTORIE

Ciclo XXXIV°

Settore Concorsuale: 05/D1

Settore Scientifico Disciplinare: BIO/09

COMPLEX, BUT FLEXIBLE NEURAL ENCODING OF ARM MOVEMENTS IN THE MACAQUE PARIETAL CORTEX

Presentata da: Francesco Edoardo Vaccari

Coordinatore Dottorato

Prof.ssa Matilde Yung Follo

Supervisore

Prof.ssa Patrizia Fattori

Esame finale anno 2021

INDEX

ABSTRACT

During life, our brain receives several stimuli coming from the outside, integrates them to build an internal representation of the world, takes decisions on the basis of this internal representation, and produces a motor behaviour. A central role in interacting with the environment is played by higher cortical areas, in which neurons are often sensitive to multiple features of the external world. This type of encoding is termed 'mixed selectivity' and greatly expands the complexity of neural representations. This phenomenon has important computational implications, since it allows a simple linear readout to generate a huge number of different potential responses and increase the generalizability of the code. On the contrary, neural representations based on highly specialized neurons would be low dimensional and it would not be possible to readout information in a flexible way, depending on the context.

Recent studies have demonstrated that neurons in parietal cortex show 'mixed selectivity' with individual cells modulated by multiple task parameters. In particular, the medial posterior parietal area V6A in the macaque is tuned by many aspects of reaching movements, thus it is likely to contain 'mixed selectivity' neurons as well. Here, we used Generalized Linear Models (GLMs) to simultaneously evaluate the contribution of several factors upon V6A cells during a fix-to-reach task and directly test this hypothesis.

The activity of 181 V6A neurons has been recorded from 2 *Macaca fascicularis* during a foveated delayed reaching task performed towards 9 different targets in the darkness. The targets were placed at eye level at different depths and directions. During the first step of the fitting procedure, LASSO optimization was used to remove from the model the regressors with a negligible influence on neural activity. Then, for each neuron, many models (the complete, several nested and a null one) were estimated and subsequently compared. This approach resulted in the definition of a 'functional fingerprint' representative of the functional properties of each unit.

First, the type of the feature encoding in V6A was studied. The analysis highlighted the virtual absence of units strictly selective for only one factor and revealed that most cells are characterized by 'mixed selectivity' with single neurons that form a continuous functional spectrum spanning from the more selective to those with a predominant mixed selectivity. The population resulted 'category free', with no evidence for any functional segregation. Second, exploiting the GLM framework, the dynamics of spatial parameters encoded within V6A were investigated. The results suggest that the spatial tuning of the population reached a peak during the movement phase, but overall a motor code is maintained along the entire task.

Finally, the intrinsic part of the model (that is the previous spiking history of the cell) resulted extremely relevant to explain the neural modulations for the majority of the cells (62%). Moreover, we observed two main trends in the encoding of the spiking history. Interestingly these trends were not ascribed to well-defined clusters of cells, but they opened the possibility that differential computations are performed different, partially overlapping sub-groups of cells. Further studies are needed to investigate this hypothesis.

In conclusion, the presence of ‘mixed selectivity’ also in area V6A, highly expected but never directly tested before, supports the growing emphasis on the importance of neurons exhibiting complex neural behaviours that are not easily attributable to the encoding of single task parameters. These emerging aspects of the neural code demand a paradigm shift to overcome the artificial concept of cell categories or classes. In practical applications, these analyses based on GLMs could improve the performances of Brain Machine Interface systems selecting the areas or the cells more suitable for the task requirements.

1 INTRODUCTION

1.1 Mixed selectivity and high dimensional neural coding

The traditional view of how the brain works is that individual neurons and even entire brain areas are highly specialized for specific functions. However, this does not explain many experimental observations, especially regarding high-order cortices. For example, after training, only one cognitive task engages almost half of the neurons in prefrontal cortex (40% of randomly chosen cells; Fusi et al., 2016). Whether in the brain there was a strict specialization, learning a second task would saturate the computational capacity of the prefrontal cortex. But since this is not the case, some more complex properties must be the basis of neuron functions.
Indeed, a growing number of authors in the neuroscience field is emphasizing the importance of neurons exhibiting complex neural behaviours that are not easily or directly attributable to the encoding of single task parameters.
The neuron capacity to respond to many different inputs is defined 'mixed selectivity' (Johnston et al., 2020; Parthasarathy et al., 2017; Fusi et al., 2016; Rigotti et al., 2013). It has been shown that the non-linear integration of these many inputs is the optimal way to encode features in a high-dimensional neural space and allow an easy read-out from downstream structures (Fusi et al., 2016).
The previous sentence implicitly contains two key points: information encoding and information decoding.
First, the expression 'neural representation', often used to mean that "the neural activity encodes, maps or refers to self-subsistent, meaningful and measurable features of the environment" (Vilarroya, 2017), assumes a coherent conversion of the information contained in the stimuli in the neural code, i.e., the firing rate of the neurons (see the paragraph Limitations in the Discussion with regard to the neural temporal code that has not been considered here). A linear mapping of the stimuli directly in the firing rate would be at a first glance the easiest way to encode such information (a neuron represents a stimulus; when the stimulus doubles, the firing rate doubles and so on). However, since the firing frequency of parietal neurons normally ranges between of 0 and 100 Hz (Maimon and Assad, 2009; Joelving et al., 2007), this type of encoding inexorably fails when the range of the stimulus is too large to be encoded in the firing rate. Non-linear encoding can prevent this response saturation, being the relation between stimulus and firing rate more flexible.
Second, the information encoded in the firing rate must be accessible for further processing. Indeed, each unit of the network needs to 'decode' the information that receives (i.e., answers the question: what do these spikes mean?), process it and pass forward what is relevant to finally produce the proper behaviour. For example, in the prefrontal cortex, where conscious decisions are taken, neurons have not direct access to the visual receptors, but they have to infer from the spikes coming from the visual areas information about

the environment. More downstream, the motor regions need to infer from prefrontal spikes which is the right action to perform and allow the body to move accordingly. The non-linear mixed selectivity serves to facilitate these processes (Fusi et al., 2016).

1.1.1 Why do neurons mix?

To understand the advantages of encoding information with mixed selectivity and nonlinear combinations of features rather than in a highly specialized way or with simple linear combinations of features, consider fig. 1. The axes represent the firing rate of three different neurons (f_1, f_2 and f_3). The first cell is linearly selective to sound intensity; the second is linearly sensitive to visual contrast and the third responds to a linear combination of the two factors. We can define the first two neurons as 'purely selective' and the third as 'linear mixed selective'. The four points in the figure represent the responses of the three neurons in four different conditions (i.e., four different combinations of the factors). The subject had to respond in one way to two of the combinations (red points) and in another way to the other two combinations (yellow). Note that, even if we are considering three dimensions, the points lay on a 2D plane, thus the neural representation of the stimuli has only two dimensions. To execute the task, a fourth downstream neuron receiving inputs from the first three should discriminate between the two appropriate responses, decoding the information contained in f_1, f_2 and f_3. The simplest possible readout, easily implemented by single units also in artificial neural networks, is a linear weighted sum and threshold operation. This would be represented in our scheme as a plane separating the red from the yellow points. With the linear neural tuning shown in fig. 1a, it is not possible to draw a plane that can separate yellow from red conditions. It could be possible to find a plane that separates one larger factor from the rest, such as all conditions with loud sounds or low contrast, but it is not possible to separate different combinations of high and low signals. Conversely, we can consider the case in which one of the neurons (the third) is a mixed selectivity neuron whose firing rate is sensitive to a non-linear combination of the two factors (sound intensity and visual contrast, fig. 1b). The addition of just this one neuron makes the neural representation three-dimensional since the four points are now the vertices of a tetrahedron. It is now possible to draw a plane that can separate any arbitrary combination of the two factors. More generally, the number of classifications that can be performed by a linear readout grows exponentially with the dimensionality of the neural representations of the inputs. As a consequence, a linear readout endowed with high-dimensional inputs can implement a much larger number of task-related responses. Note that also neural representations based on highly specialized or linear mixed selectivity neurons are capable to encode relevant information for one context, but these representations would result low-dimensional, preventing an easy readout in other contexts and a flexible, downstream processing of the encoded information.

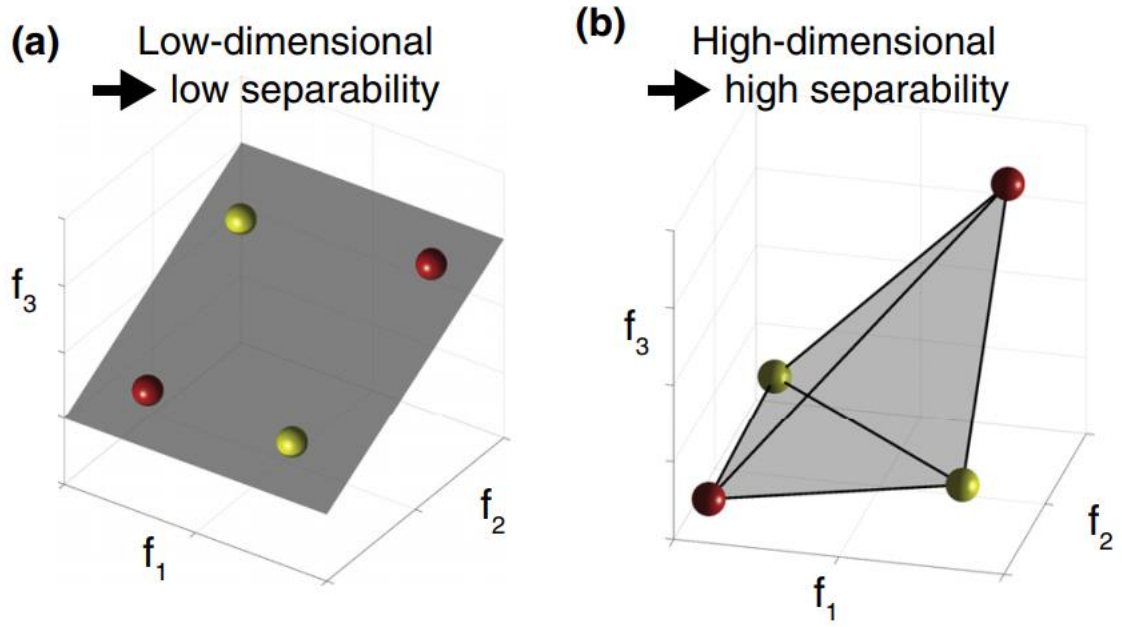

Fig. 1. Low and high-dimensional neural representations. The activity of a neuronal population of three neurons is represented as a point in the neural space. The three axes represent the firing rates fk (k = 1, 2, 3) of the three neurons. The four dots represent the population responses in four distinct experimental conditions (e.g. the responses to four sensory stimuli). The dimensionality of the neural representations is the minimal number of coordinate axes that are needed to specify the position of all points. (a) The points lie on a plane, thus the neural representation is low dimensional (2D). (b) A high-dimensional neural representation: same as in panel (a), but now the four points representing the sensory stimuli are no longer coplanar and they span three dimensions. This representation has the maximal dimensionality. In (a) a linear readout cannot be trained to separate the red from the yellow points as they all lie on a plane. This is because a linear readout can be trained only if there exists a plane (a hyperplane in higher dimensional spaces) that separates the elements that must be classified in different categories, which is clearly not the case here. Vice versa, in b) the resulting tetrahedron can be decoded by a linear classifier (note that other arbitrary chosen categories can be separated). Adapted from Fusi et al., 2016.

Another advantage of the non-linear selectivity is the reliability of the resulting neural code. Since the brain does not operate in low-noise regime (i.e., the spiking responses are highly variable), a reliable neural code must be robust to noise. It has been demonstrated that codes with a certain degree of stimulus features mixing provide great benefits to coding reliability with respect to codes without features mixing (Johnston et al., 2020). This helps to explain the ubiquity of mixed selectivity within sensory (Finkelstein et al., 2018; Rentzeperis et al., 2014; Walker et al., 2011), frontal (Fusi et al., 2016; Rigotti et al., 2013), and motor cortices (Churchland and Shenoy, 2007; Hatsopoulos et al., 2007).

It seems that, the cortex, or maybe the entire brain, processes information based on the conjunctive coding for multiple stimulus features, thus new approaches have to be taken and attention should shift to cells with the most complex behaviours. But how does this new framework reconcile with past findings about highly specialized neurons? In the context of the mixed selectivity, since information is randomly distributed in the

population (i.e., the set of features encoded by each cell is different and random) and each neuron responds differently to different stimuli, the emergence in the network of a highly specialized unit can occur by chance, but this case would be just an epiphenomenon, representing an exception rather than the rule. For this reason, considering these few neurons with an easily identifiable activation pattern as representative of the functional properties of a neural population could be misleading.

1.1.2 Where does the 'mixed selectivity' come from?

A relevant key-point is how the mixed selectivity is biologically implemented in the network of interconnected neurons. In recent computational models, it has been observed that the dimensionality of the neural representations is expanded by nonlinearly mixing the different sources of information in a population of randomly connected neurons (Pascanu et al., 2011; Rigotti et al., 2010; Buonomano et al., 2009; Sussillo and Abbott, 2009; Jaeger et al., 2004; Maass et al., 2002). Interestingly, a similar random connectivity has been suggested on the basis of anatomical reconstructions (Braitenberg and Schüz, 1998). If on one side, a single layer of randomly connected neurons is sufficient to implement a nonlinearly mixed code, dendritic spines could play a central role in this process on a micro-scale (Barak et al., 2013). In fact, exploiting intrinsic nonlinearities, a single branch of the dendritic tree could act as an additional hidden unit of the network of randomly connected neurons (Barak et al., 2013). Some features of the dendritic spines support the idea that they participate in building plastic, distributed circuits (Yuste et al., 2011). Moreover, on the meso-scale, these mixed selective responses likely converge on brain structures with specific functions, explaining how the apparent chaos of the former can finally trigger the stereotyped activity of the latter (Mittal et al., 2020; Sosulski et al., 2011).

1.2 The posterior parietal cortex and the mixed selectivity

In the past, the posterior parietal cortex (PPC) was classically defined an 'association cortex' and viewed as a structure mainly dedicated to the integration of different types of sensory information. Then it became evident that, besides the integration of different sensory modalities, especially somatic and visual, this cortical region was strongly involved also in the control of movements, gaze and visuospatial attention (Hadjidimitrakis et al., 2019; Galletti and Fattori, 2018; Pisella et al., 2017; Caminiti et al., 2015; Sereno and Huang 2014; Filimon, 2010; Galletti et al. 2010, 2003; Andersen and Cui, 2009; Gottlieb, 2007; Andersen et al., 1997; Kalaska, 1997).

Given the plethora of features that have an influence on posterior parietal areas, a question arises spontaneously: is the encoding of these neurons characterized by mixed selectivity or, in contrast, do highly specialized sub-populations of cells exist?

Recent studies have demonstrated that neurons in parietal cortex have “mixed selectivity”, thus individual neurons are modulated by multiple task parameters. In mice, PPC neural activity during a virtual-navigation decision task was not attributable to classes of specialized cells, but rather to high-dimensional dynamics (Harvey et al., 2012). Also within rat PPC, during a multisensory decision making task, the neural population it has been shown to be category-free and response features were randomly distributed across neurons (Raposo et al., 2014). In the macaque, in which PPC segmentation is more clearly defined, the lateral intraparietal area (LIP) hosts extremely heterogeneous neurons, mainly involved in saccades planning / execution, in processing visual stimuli, but also in decision making and evidence accumulation (Premereur et al., 2011; Andersen and Cui, 2009). Indeed, many cells resulted modulated by both non-spatial category and spatial saccade related signals (Rishel et al., 2013; Freedman and Assad, 2009). Moreover, LIP neurons mix decision signals with decision-irrelevant signals (Meister et al., 2013), in accordance with the high-dimensionality of neural representations expected in the context of mixed selectivity (see above).

Another PPC section, the anterior intraparietal area (AIP), is known to be modulated by hand shape during grasping (Murata et al., 2000), visual object properties (Romero et al., 2014, 2012; Rizzolatti and Luppino, 2001), context-specific hand grasping movements (Baumann et al., 2009), but also gaze and reach target positions (Lehman and Scherberger, 2013). Recently, Zhang and colleagues (2017) found that the human homologue of macaque AIP showed a ‘partially’ mixed selectivity. In this particular case, the task features were randomly distributed in the population, except for the effector of the action (hand or shoulder). The other variables (body side and strategy) were mixed only within, but not between, effectors (see fig. 2). This encoding structure was robust and maintained across different conditions (open vs. closed loop in an experiment involving a brain machine interface; Zhang et al., 2020).

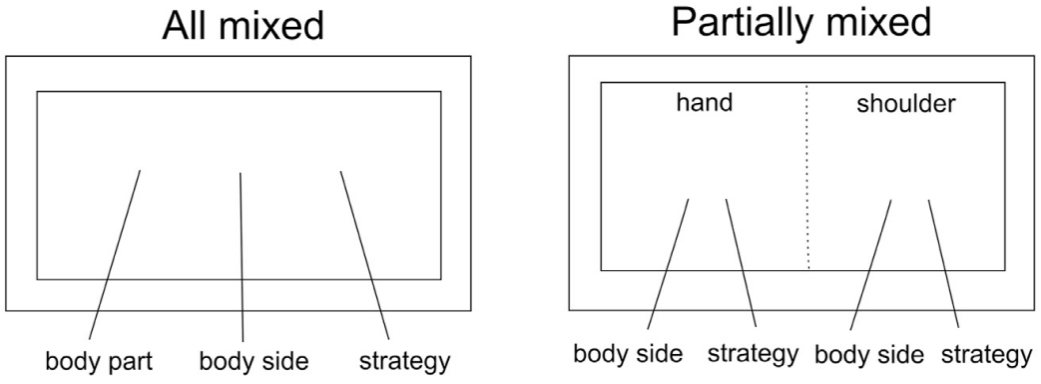

Fig. 2. Possible organizational models of neural mixed representations (a) The neural population exhibits mixed selectivity, with individual neurons showing tuning to various conjunctions of variables. The variables are randomly distributed across the entire population. (b) The neural population exhibits partially mixed selectivity, with the mixing of representations being dependent on the variables under investigation. Here, hand and shoulder are encoded by segregated sub-populations (i.e., a unit can encode hand OR shoulder, not both); however, the other variables (body side and strategy) are mixed within, but not between, effectors. Note that solid lines in this diagram indicate anatomical boundaries of neural populations, while dotted line indicates functional boundaries/segregation. Adapted from Zhang et al., 2017.

1.3 The posterior parietal cortex and V6A area

The frontoparietal network controls movements and it has been preserved in primates and humans (Ghahremani et al., 2017). Within this network, a fundamental node for reaching is represented by the PPC. In the literature related to monkey PPC, references to the so-called 'Parietal Reach Region' (PRR) are often found, especially by American authors. In a few words, the PRR is a functionally defined region in which most neurons are sensitive to the direction of reaching movement (Snyder et al., 2000, 1997; Batista et al., 1999). Anatomically, this region includes part of the anterior bank of the parieto-occipital sulcus (POS) and the medial bank of the intraparietal sulcus (Battaglia-Mayer et al., 2000; Snyder et al., 1997; Kalaska et al., 1983), mainly overlapping with areas V6A and MIP (Medial IntraParietal area).

Nowadays, even if the debate on which can be the best parcellation of the PPC is still ongoing, many areas have been further identified with both functional and cyto-architectonic criteria (Gamberini et al., 2020; Cavada, 2001), therefore for clarity and precision, in this thesis the nomenclature of the single areas will be used. Among the areas that compose the PPC of the macaque, one that certainly stands out for the multitude of its functional properties is area V6A (see Galletti and Fattori, 2018; Fattori et al., 2017, for reviews). The next paragraphs will provide a brief overview of the main features of this region.

From an anatomical point of view, area V6A, firstly identified in seminal works by Galletti and collaborators (Luppino et al., 2005; Galletti et al., 1999, 1997, 1996), occupies the dorsal part of the anterior bank of POS (see fig. 3). It is delimited posteriorly by visual area V6; laterally by MIP; anteriorly by PEc; medially by PGm.

Area PO has sometimes been mistakenly confused with V6A. Indeed, historically, the whole anterior bank of the POS constituted the PO area, thus encompassing both areas V6 and V6A, according to its original description (Gattass et al., 1986; Covey et al., 1982). However, subsequently other authors used the same terminology (area PO) to define different cortical sectors: for example, the restricted PO of Colby and colleagues (1988) occupied only the ventral part of the anterior bank of POS, mostly overlapping with area V6 and not with area V6A (see Galletti et al., 2005; Cavada, 2001). In our definition, area PO and V6A partially overlap, but they do not represent the same area, being V6A a well-defined part of PO.

Recently, the human homologue of the macaque V6A has been identified in the vicinity of the POS (Pitzalis et al., 2015, 2013). Human V6A shares functional properties almost completely overlapping with monkey V6A (see next paragraphs), such as the activation for finger pointing and reaching movements (Tosoni et al., 2015), differently to what it has been observed for human V6 (Pitzalis et al., 2010, 2006).

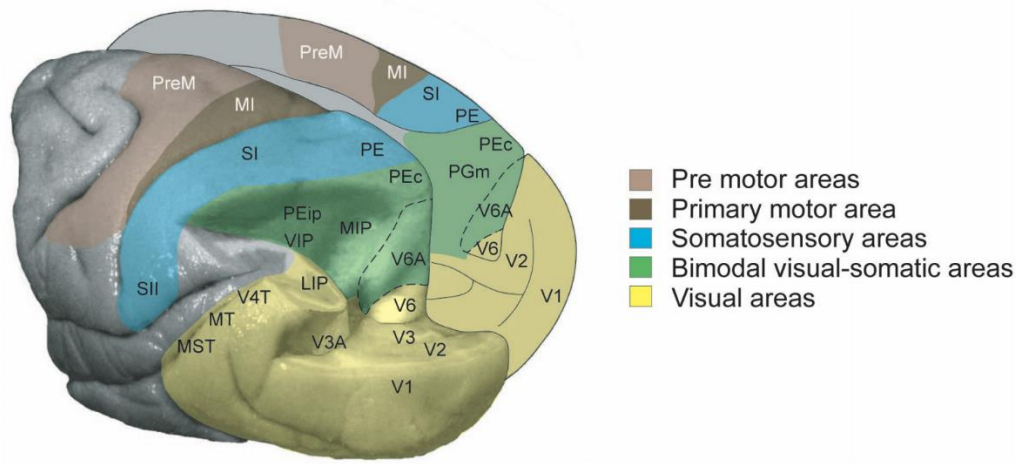

Fig. 3. Cortical areas of the macaque brain. Left: postero-lateral view of a partially dissected left hemisphere with a part of the inferior parietal lobule and of the occipital lobe cut away in order to show area V6A hidden in the parieto-occipital sulcus. Right: medial view of the right hemisphere. Labels on different brain regions indicate cortical areas according to anatomical and functional criteria. Colors indicate sensory or motor properties of different regions of the brain. Note that area V6A is at the posterior end of the bimodal (visual/somatosensory) region and borders the visual areas of the occipital pole. Adapted from Fattori et al., 2007.

Fig. 4 shows V6A cortico-cortical connections. Briefly, it is bi-directionally connected with the dorsal premotor areas F2 and F7 (Passarelli et al. 2011; Gamberini et al. 2009; Marconi et al., 2001; Caminiti et al., 1999; Shipp et al. 1998; Matelli et al. 1998), as well as with several visual and parietal areas. V6A receives inputs from the visual areas of the occipital lobe (V2, V3, V4, MST, V6) and from the multimodal (visuomotor, somatomotor…) areas AIP, LIP, PEc and MIP (Bakola et al. 2017, 2010; Marconi et al., 2001; Caminiti et al., 1999).

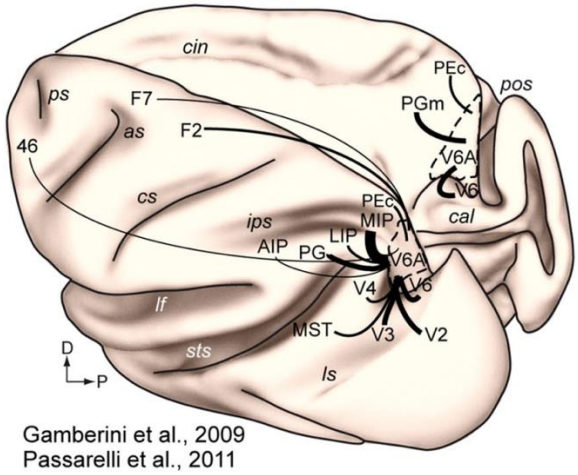

Fig. 4. Summary of the main cortico-cortical connections of area V6A. Only projections representing more than 1% of the total cortical connections are reported. The thickness of connecting lines is proportional to the strength of connections. Abbreviations: D dorsal; P posterior; ps principal sulcus; as arcuate sulcus; cin cingulate sulcus; cs central sulcus; lf lateral fissure; ls lunate sulcus; sts superior temporal sulcus; ips intraparietal sulcus; cal calcarine sulcus; pos parieto-occipital sulcus. Adapted from Gamberini et al., 2020.

1.3.1 Visual properties of V6A area

V6A lays within Brodmann area (BA) 7, just anteriorly to the contiguous area V6 (BA 19) that is characterized by visual responses (Gamberini et al., 2020). Although the strong connections from V6 to V6A, a number of physiological properties distinguish the two areas (Galletti et al., 1996). In particular, V6A contains units with craniotopic receptive fields ('real-position' cells), units tuned to very slow stimulus speeds, units with complex visual selectivity and units exhibiting attention related activity (Galletti et al., 2010, 1999, 1993). V6A was also found to have a larger (20-35°, Galletti et al., 1999) mean receptive field size than V6. Overall, 60% of V6A neurons were found to be visually responsive (Gamberini et al., 2011). These were divided into 'low-level visual' if they responded only to simple stimulations, 'high-level visual' if they responded to complex stimulations. 'High level' units were mainly located in the dorsal part of the area, while 'low level' ones were mostly present in the ventral part (Gamberini et al., 2011).

Generally, the receptive fields of V6A neurons cover the entire visual field with a poor retinotopic organization. Representation of the inferior contralateral quadrant, from the fovea to the periphery, is particularly present (fig. 5A). Interestingly, many V6A receptive fields encompass the two hemifields. These findings are in accordance with V6A role in the control of actions performed by the arm and the hand. It has been shown that when a visual stimulus appears in the lower part of the visual field, pointing (Danckert and Goodale, 2001) or grasping (Brown et al., 2005) actions are faster and more accurate. Note that the part of the visual field most represented in V6A overlaps perfectly with the region of space traversed by the hand and arm when reaching for an object that is being fixed with the fovea (fig. 5B).

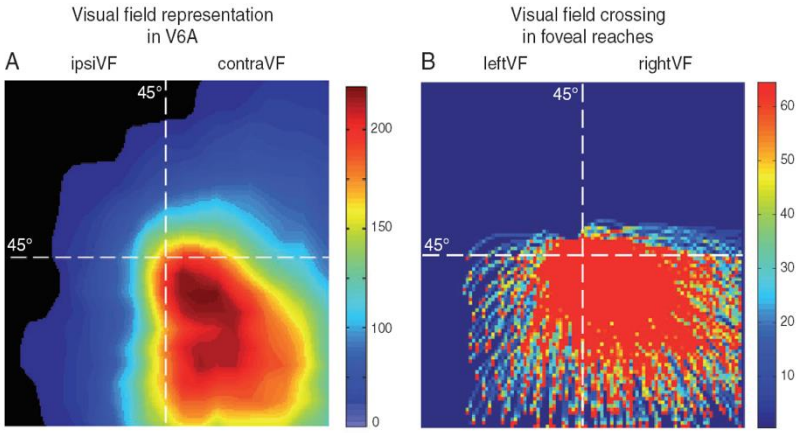

Fig. 5. Representation of the visual fields of V6A neurons (A). The color scale indicates the density of visual fields covering that specific part of the visual field. In the dark red area, more than 200 visual fields overlap among those recorded. IpsiVF, ipsilateral part of the visual field. ContraVF, contralateral part of the visual field. (B) Arm trajectories of human volunteers while performing reaching movements toward objects observed with the foveal area of the eye. All trajectories are plotted overlapping the object position: ipsiVF and contraVF are respectively the ipsilateral and contralateral part of the visual field with respect to the arm used. A strong correspondence between the visual field representation of V6A and the part of the visual field crossed by the arm during reaching is evident. Adapted from Fattori et al., 2017.

1.3.2 Oculomotor properties of V6A

It was demonstrated that V6A neurons activity also reflect oculomotor behaviour. About 48% of visual and 32% of non-visual neurons showed eye position-related signals in total darkness (Galletti et al., 1995). In addition, the majority of visual responses (60%) was modulated by gaze position. The sensitivity of many cells for elevation and version of the gaze is shown in fig. 6 (Galletti et al., 1995), but also modulations for the vergence (tightly related to the depth) have been found more recently (Breveglieri et al., 2012). Eye position modulations were different from cell to cell, spanning from large, planar fields to peak-shaped fields localized in restricted regions of the field of view (Nakamura et al., 1999; Galletti et al., 1995).

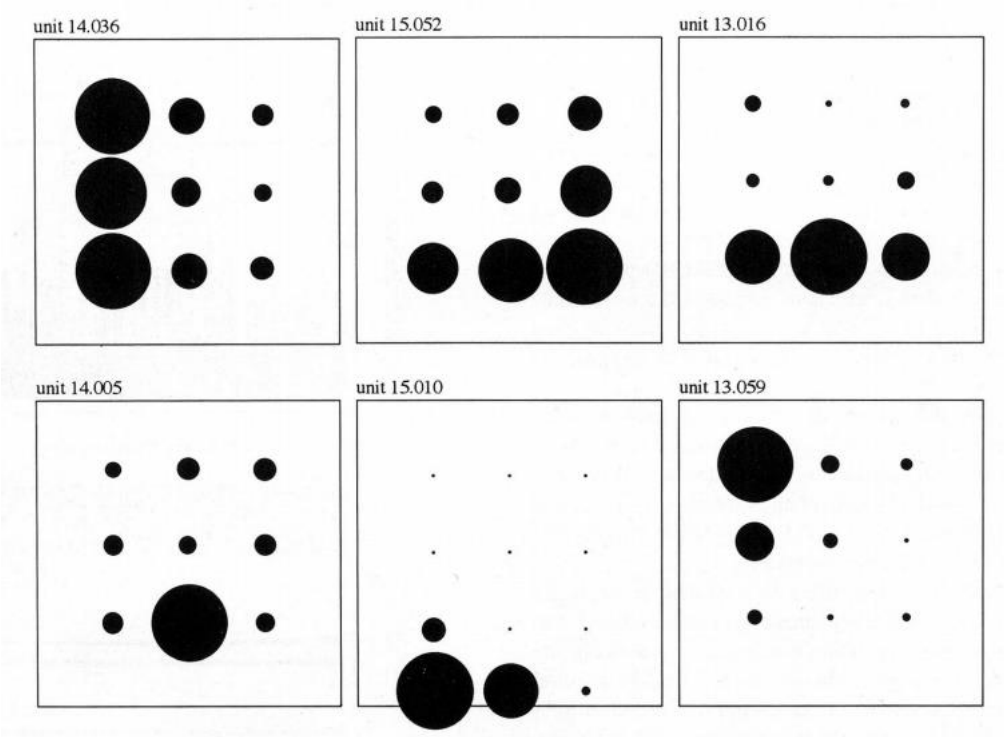

Fig. 6. Eye position related activity of six V6A neurons. Tests were performed in complete darkness. Squares represent the screen facing the animal. Activity of the cells recorded while the animal looked at different screen locations is reported as dark disks whose diameter is proportional to the firing rate of discharge. Adapted from Galletti et al., 1995.

A lower, but still significant, proportion of V6A cells shows modulation for saccades, exhibiting both pre- or post-saccadic activity (Kutz et al., 2003; Battaglia-Mayer et al., 2001, 2000). These responses can be strongly spatially tuned, as shown in fig. 7.

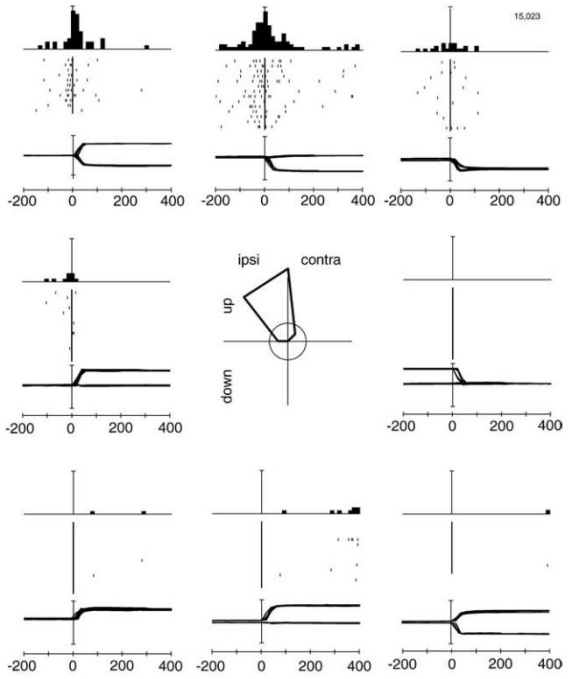

Fig. 7. Sensitivity of a V6A saccade-related cell to the direction of saccade. Each of the eight figures surrounding the central polar plot shows, from top to bottom, the peri-saccade time histogram raster-plot, and eye-traces aligned to saccade onset (t=0 ms, bin width 15 ms). Each figure is located in the same position as the peripheral target of saccade with respect to the central starting position (see Methods). Central figure is polar plot of the direction sensitivity (mean activity for each direction); ipsi ipsilateral direction of saccadic movement, contra contralateral direction, up upward direction, down downward direction. Scale bars: in histograms 75 spikes/s; in eye-traces 60°; Scale circle in polar plot indicates activity of 15 spikes/s. Adapted from Kutz et al., 2003.

V6A could receive gaze position signals from neighbouring PPC areas that encode eye movements and fixations in depth and with which it is strongly connected, like LIP and area 7a/PG (Passarelli et al., 2011; Gamberini et al., 2009). An alternative hypothesis, not mutually exclusive with the previous one, is that the modulations for vergence and version are already embedded in the visual information that V6A receives from visual areas, since similar responses have been found in single neurons (30–50%) at early nodes of the visual stream (V1, V2 and V4; Rosenbluth and Allman, 2002).

1.3.3 Somatosensory properties of V6A

Visual information is not the only sensory information that reaches area V6A. This area also receives contralateral somatic stimuli mainly from the upper limbs (Breveglieri et al., 2002). Approximately 30% of V6A cells respond to tactile or proprioceptive stimulation. Most somatosensory cells have the somatic receptive field on the proximal part of the arm, with the remainder on the distal part and the hand (fig. 8). Proprioception (i.e., joint position) is more represented than touch (75% vs 25%). Among proprioceptive inputs, the most represented are the shoulder, the elbow and the distal arm joints (wrist and fingers; Gamberini et al., 2018, 2011). Somatosensory responses are found mainly in the dorsal part of V6A, where in contrast visual cells have a lower incidence. The representation of the body is not somatotopically organized and incomplete. Head and legs are completely missing, represented instead in other areas such as VIP for the head (Graziano and Cooke, 2006; Sereno and Huang, 2006; Duhamel et al., 1998) and PEc and PE for the legs (De Vitis et al., 2019; Seelke et al., 2012; Breveglieri et al., 2006; Taoka et al., 2000). It is worth noting that active arm movements have been found to be more effective than passive movements in activating V6A neurons (see next paragraph).

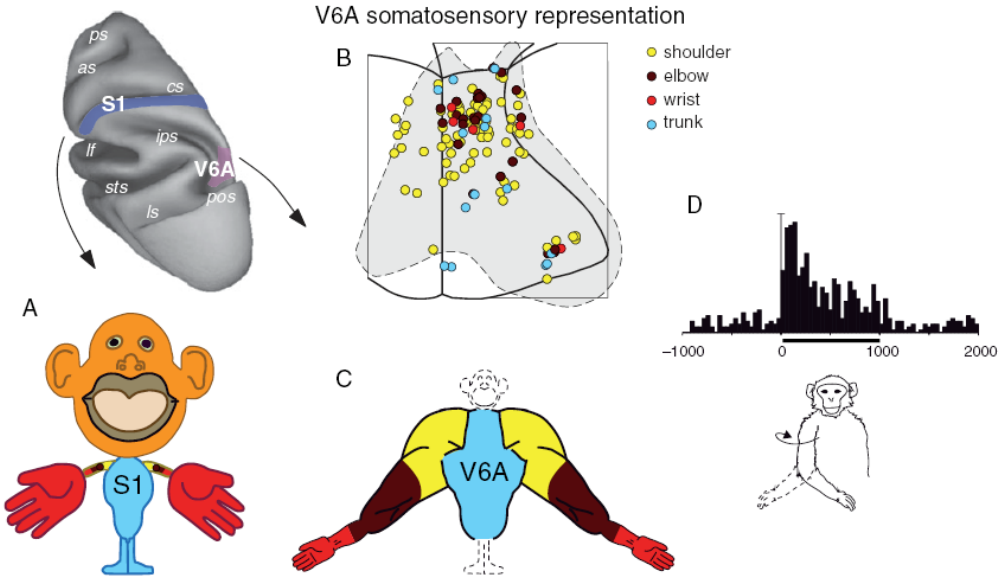

Fig. 8. Somatosensory representation in V6A. (A) Top: dorsolateral view of the macaque brain where areas S1 and V6A are shown in blue and pink, respectively. (A) Bottom: homunculus in area S1 showing body representation from both hemispheres. (B) 2D map of V6A showing the locations of the neurons whose receptive fields were used to draw the homunculus in V6A. (C) Homunculus in V6A area reporting the body representation from both hemispheres. Note the over-representation of the torso and shoulders and the lack of head and legs. (D) Neuronal response of a somatosensory cell of V6A. The response is represented by a peristimulus histogram aligned on the onset of stimulation (Passive Shoulder Rotation). This cell was responsive to arm abduction as depicted in the figure, but not to the opposite movement. Adapted from Fattori et al., 2017.

1.3.4 Motor properties of V6A: reaching movements

As described above, area V6A is part of Brodmann's area 7, which belongs to the visual associative cortex and responds accordingly to visual stimuli. Quite unexpectedly for that time, V6A was found to show a strong reaching activity (Galletti et al., 1997). Initially this was demonstrated by making the monkey perform stereotyped and repetitive movements of the arm in complete darkness, so that the arm itself was out of its visual field, while the animal kept its gaze fixed on a fixation point. Under these experimental conditions, it was observed that approximately 60% of V6A cells showed activity related to arm movement. It is noteworthy that neural activity often preceded the first electromyographic response so it could not be related to possible sensory feedback stimuli from the moving arm (Galletti et al., 1997).

After this first report, further experiments studied more deeply the motor properties of this area showing that the activity is modulated by the direction in which the movement occurs (Fattori et al., 2005; Battaglia-Mayer et al., 2001). Comparing the timing of neuronal discharges with muscle activity, it was found that about 70% of cells discharge before the onset of movement and about 20% of these even before the onset of the earliest electromyographic activity (Fattori et al., 2005). At least for these latter neurons, neuronal discharges cannot be traced to somatosensory stimuli. It is possible, instead, that this reaching-related activity is based on copies of efferent signals sent to V6A by motor centres, such as the dorsal premotor areas F2 and F7, which are directly and reciprocally connected with V6A (Passarelli et al., 2011; Gamberini et al., 2009; Matelli et al., 1998).

On the other side, the discharges observed after electromyographic activity and, in particular, after the onset of movement could also be explained by somatosensory stimuli arising, for example, from movements of the joints.

Comparing neuronal responses to reaching under dark and light conditions, the discharges reflect motor and somatosensory inputs (dark condition), whereas they also incorporate visual feedback from the moving arm (light condition; Bosco et al., 2010). It was then possible to assess the weight of visual modulation and to divide the cells into 3 main categories: motor, visuomotor '+' and visuomotor '-' neurons (see fig. 9 for examples). Motor cells show equivalent activity under light or dark conditions, receiving no visual information while performing the task. Visuomotor ‘+’ cells respond more strongly to reaching in the light than in the dark, showing positive modulation (increased discharge) for visual information. Visuomotor '-' cells, on the other hand, discharge less under light than dark condition because they are partially inhibited by visual stimuli. The presence of these 3 response profiles suggests that V6A acts as a state comparator, constantly comparing the motor plane with the sensory feedback (visual and somatosensory) produced by movement (Bosco et al., 2010).

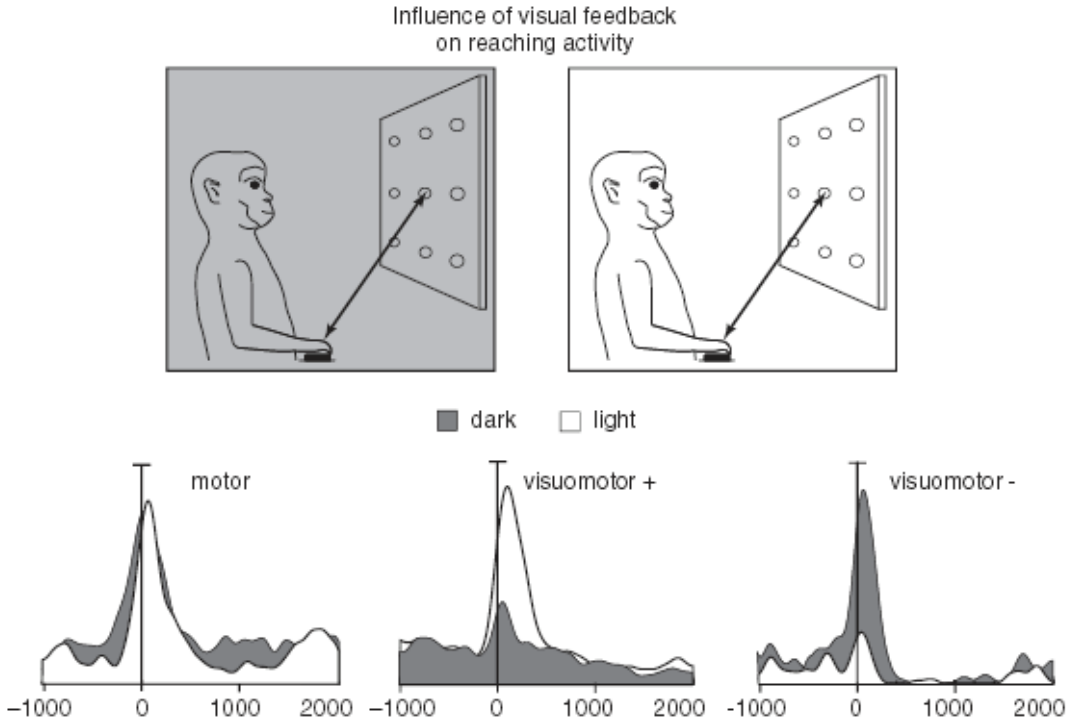

Fig. 9. Influence of vision on reaching activity in V6A. Top: drawing of the experimental light conditions where reaching was performed: complete darkness (left) and in the light (right). Bottom: response of 3 types of neurons during reaching movements in the light (white) and in the dark (gray) toward the central panel position. 3 categories of neurons are shown: motor, visuomotor + and visuomotor -. Activity is aligned on the onset of the reaching movement. Adapted from Bosco et al., 2010.

Since the findings presented so far support the role of area V6A in visuo-motor transformations and arm movements guidance, one could expect that the neural activity would be modulated also during the movement planning phases (Battaglia-Mayer et al., 2000), during which theoretically part of these processes take place. Coherently, three types of neurons have been found: cells where delay activity was equally spatially tuned for gaze position only (Gaze cells), cells partially tuned only during reaching preparation (Set cells), and cells influenced by both gaze and reaching preparation (Gaze/Set cells; Breveglieri et al., 2014). Moreover, V6A neurons could exhibit a spatial modulation only during movement preparation (10%), only during movement execution (17%) or both during preparation and execution (60%). The spatial selectivity for most cells modulated both during preparation and execution was congruent during the two task phases. Fig. 10 shows the activity of these three last sub-populations of cells.

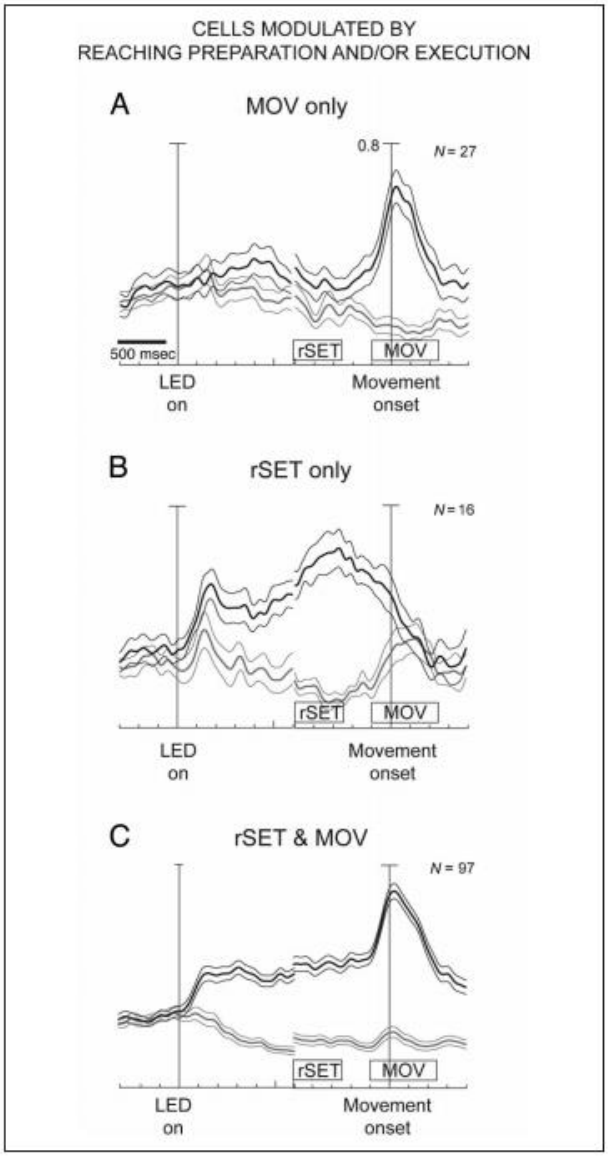

Fig. 10. Population activity of cells modulated by movement execution and/or preparation. Average normalized SDFs of cells modulated only by movement execution (A), only by movement preparation (B), and by both (C). For each cell category, the population activity for conditions with maximal (black) and minimal (gray) discharge are plotted as spike density functions (SDFs; for more details, see Breveglieri et al., 2014) . Conditions were sorted by activity in MOV (A and C, right) and during delay (B and C, left). Scale bar in all SDF plots: 80% of normalized activity. Alignment on LED and Movement onsets. 'rSET' epoch: last 500ms before the go signal. 'MOV' epoch: from 200ms before movement onset to movement end. Adapted from Breveglieri et al., 2014.

2 AIM OF THE STUDY

Given the multitude of factors that influence V6A neural activity and the mixed selectivity observed in areas that have similar type of encoding (multiple stimuli, neurons with complex behaviors etc.), an open question remains: is there mixed selectivity in area V6A?

In some of the previous V6A studies, the influence of pairwise parameters has been studied, as for instance target and gaze positions (Marzocchi et al., 2008), target position and visual condition (Bosco et al., 2010), target and initial hand positions (Hadjidimitrakis et al., 2017), etc. Recently, Bosco et al. (2019) used a novel dimensionality reduction method (dPCA) to extract from V6A information about a number of different modulating signals (visual condition, target position, wrist orientation, grip type), obtaining a compact view of the population activity. However, the question about the presence of mixed selectivity in V6A was not directly addressed so far.

To our knowledge, no comprehensive work has yet tried to correlate V6A single cell activity with a full set of modulating variables concurrently acting upon the same neuron, and during the execution of the same task. Because of the multimodal nature of V6A, we expected that its neurons are characterized by 'mixed selectivity'. Moreover, given the sensory-motor transformations occurring in this area, we also expected that the influence of spatial parameters changes over time. To test our hypotheses, we first disentangled the different parameter contributions at single cell level, then we moved to population level to study the dynamics of these contributions.

Among the mathematical probabilistic models, the family of Generalized Linear Models (GLM) offers a valid statistical framework to assess how a variable of interest (i.e., the neural activity) is explained by several features or 'regressors'. Since the Poisson distribution is the most appropriate to model single cell activity (see Methods), we used a Poisson GLM to study the effect on neuronal activity of the many factors that are known to modulate V6A. We collected spiking activity of V6A neurons and gaze positions during a delayed reaching task, then fitted neural activity of a single cell with eye-related and reaching-related parameters. Our analysis allowed us to represent activity modulations of each cell with a set of weights that we named 'functional fingerprint'.

Across the population, units were not clustered in homogenous groups according to their fingerprints, but were distributed in a functional continuum, suggesting that V6A is characterized by 'mixed selectivity'. Influences of spatial parameters were not static but changed through space and time, indicating the occurrence of visuo-spatial transformations helpful to guide movement.

3 MATERIAL AND METHODS

The current study consisted in an extended computational analysis of neural data reported previously (Breveglieri et al., 2014). Accordingly, the procedures described herein focus on analytical treatment of the data and provide only essential details of the behavioural and electrophysiological procedures. Full details of experimental methods are provided in previous published papers (Gamberini et al., 2018; Breveglieri et al., 2014; Galletti et al., 1995).

The study was performed in accordance with the guidelines of the EU Directives (86/609/EEC; 2010/63/EU) and the Italian national law (D.L. 116-92, D.L. 26-2014) on the use of animals in scientific research. Protocols were approved by the Animal-Welfare Body of the University of Bologna. During training and recording sessions, particular attention was paid to any behavioral and clinical sign of pain or distress.

3.1 Experimental Procedures

Two male macaque monkeys (Macaca fascicularis) weighing 4.4 kg (M1) and 3.8 kg (M2) were used. Single cell activity was extracellularly recorded from the anterior bank of the parieto-occipital sulcus (POs). The electrodes entered directly into the cortex of the exposed surface of the caudal aspect of superior parietal lobule or passed through the occipital pole and the POs to reach the anterior bank of the sulcus in the depth (inclination angle of electrodes was 30-32°posteriorly from the coronal plane). After passing through areas V1–V2 of the occipital lobe, the electrode reached the anterior bank of the POs at a variable depth (up to 8mm) according to the anteroposterior coordinate of penetration. Area V6A was initially recognized on functional grounds following the criteria described in (Galletti et al. 1999) and later confirmed based on the cytoarchitectonic criteria of (Luppino et al. 2005).

We performed multiple electrode penetrations using a five-channel multielectrode recording system (Mini Matrix, Thomas Recording GmbH, Giessen, Germany). The 5 electrodes of the Mini Matrix were 200 µm spaced. Each penetration consisted of the insertion of the electrodes through the holes (1x1 mm) of a circular grid (18mm diameter) located in the recording chamber. The coordinates of the circular grid were used to reconstruct the locations of the recorded neurons. The electrode signals were amplified (at a gain of 10,000) and filtered (bandpass between 0.5 and 5 kHz). Action potentials in each channel were isolated with a waveform discriminator (Multi Spike Detector; Alpha Omega Engineering Nazareth, Israel) and were sampled at 100 kHz. Quality of single-unit isolation was determined by the homogeneity of spike wave forms and clear refractory periods in ISI histograms during spike-sorting. Only well-isolated units not changing across tasks were considered. The animal behaviour was controlled by custom-made software implemented in LabVIEW (National Instruments, Austin, TX) environment (Kutz et al. 2005). Eye position signals were sampled with

two cameras (one for each eye) of an infrared oculometer system (ISCAN, Woburn, MA) at 100 Hz. The vergence angle was not recorded online, but it was reconstructed offline from the horizontal eye positions of the two eyes. A sort of control for vergence resulted from the presence of electronic windows (one for each eye, 4° × 4° each) that controlled the fronto-parallel gaze position, so that we could set an offset of the horizontal eye position signal for targets located in the same direction, but at different depths.

3.2 Behavioural Task

Electrophysiological signals were collected while the monkeys were performing an instructed-delay body-out reaching task (fig. 11). The targets were located in different positions in the 3-D space. During the task the animals were fixating a target that they would reach when instructed. Monkeys sat in a primate chair, with the head restrained, and faced a horizontal panel located at eye level. Nine light-emitting diodes (LEDs) mounted on the panel at different distances from the eyes were used as fixation and reaching targets. As shown in fig. 11A, the target LEDs were arranged in three rows: one central, along the sagittal midline, and two laterals, at isoversion angles of −15° and +15°, respectively. Along each row, three LEDs were located at isovergent positions of 17.1°, 11.4°, and 6.9°, respectively. The two animals had the same interocular distance (3.0 cm), so we placed the isovergent rows at the same distance from the monkeys in both animals (nearest targets: 10 cm from monkey eyes; intermediate targets: 15 cm; far targets: 25 cm). The range of vergence angles was chosen to be within the limits of peripersonal space, so the monkeys were able to reach all target positions. The animals performed the task with the limb contralateral to the recording site while maintaining steady fixation. The hand started the trial pushing a button (home button, 2.5 cm in diameter, fig. 11A, B) placed outside the monkeys' visual field, 5 cm in front of its trunk. 1000 ms after home button pressing one of the 9 LEDs lit up green. The monkeys were required to fixate the fixation point while keeping the button pressed. The fixation point served as a cue concerning the direction of the arm movement to perform. However, the monkeys needed to withhold the instructed behaviour without performing any eye or arm reaching movement for 1700–2500 ms, till the change in colour of fixation LED (green to red). The colour change of fixation target was the go signal for the animal to release the home button and start an arm movement toward the target. The monkeys had 1 sec after the go signal to reach the target; otherwise, the trial was aborted. Then, monkeys pushed the target and held the hand on it for 800–1200 ms. The target offset cued the monkeys to release the LED and return to the home button, which ended the trial and allowed monkeys to receive reward. Notice that since target offset, the animals were allowed to break fixation. Only correctly executed trials were used in this analysis.

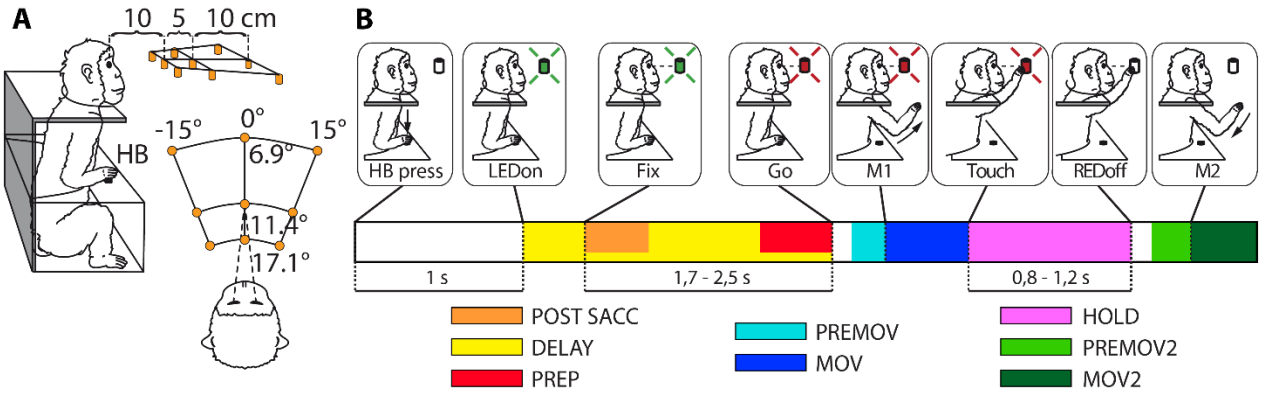

Fig. 11. Schematic representation of the task. (A) Experimental setup. Reach movements were performed in darkness toward 1 of 9 LEDs (orange) arranged over a panel mounted at eye level in front of the monkey. Spatial coordinates of targets are indicated as vergence and version angles with respect to the eyes. HB: Home Button. (B) Task sequence. From left to right: trial start (HB press), target appearance (LEDon), fixation onset (end of saccade, Fix), go signal (Go), start of the arm movement (M1), touch and holding of the target (Touch), LED switch-off (REDoff) return movement (M2). Color bar below the drawings illustrate the epochs considered in the model. DELAY epoch overlaps with POSTSACC and PREP. Adapted from Diomedi et al., 2020.

3.3 Poisson GLM and LASSO optimization

Generalized linear models (GLMs) are a flexible generalization of ordinary linear regression used for variables that have distribution other than Gaussian. In this sense, ordinary linear regressions can be seen as a specific type of GLM.

In premotor (Takahashi et al., 2017) and somatomotor cortex (Goodman et al., 2019; Hatsopoulos et al., 2007), for instance, GLMs (or ordinary linear regressions) provided interesting insights about the neural modulations for several kinematic parameters of the upper limb. In different contexts, also gaze position can be included in these models (Lehmann and Scherberger, 2013).

Poisson distribution is used for modelling the number of times that an event occurs in an interval of time. So, the behaviour of a neuron (i.e.,variations of its spiking activity) can be modelled as a Poisson process (Triplett and Goodhill, 2019; Pillow et al., 2008; Truccolo et al., 2005; Paninski et al., 2004b; Dayan and Abbott, 2001). Thus, the probability of observing the spike count y from a neuron in a short period of time is:

$$P(y|\mu,\Delta) = \frac{e^{-\mu\Delta}\mu\Delta^{y}}{y!}$$

where μ represent the firing rate over unit time and Δ is the bin width.

GLM with Poisson distribution assumes that the varying firing rate at a specific time t can be represented as the exponential of the linear combination of the parameters called regressors, and so:

$$\mu_t = \exp(\beta_0 + \beta_1 X_{1,t} + \ldots + \beta_K X_{K,t})$$

where K is the number of regressors, $\{\beta_k\}_{k=1,\ldots K}$ are the regression coefficients, each$X_{k,1\ldots T}$ is a vector of regressors and β_0 is the constant of the model.

The regression coefficients are estimated through a procedure called Maximum Likelihood Estimation (MLE) that maximizes the log-likelihood (the logarithm of the likelihood, computationally easier to calculate), i.e.,the probability, given a model, to observe a given spike train. The log-likelihood function for Poisson GLMs can be calculated as:

$$\ell(y, \beta) = \log[L(y, \beta)] = \sum_{t=1}^{T} y_t \log(\mu_t) + \sum_{t=1}^{T} y_t \log(\Delta) - \sum_{t=1}^{T} \log(y_t!) - \Delta \sum_{t=1}^{T} \mu_t$$

where Δ is the bin width. We followed a procedure similar to the one recently adopted by Goodman and colleagues (2019). In a first phase of the fitting, we applied an optimization method called LASSO, commonly used when a model includes many regressors and their correlation with the dependent variable is not know *a priori.* This is used to avoid over-fitting and to select the more significant regressors because it shrinks the size of the regression coefficient and sets the unimportant ones to zero. For this aim, we added the LASSO penalty term to the log-likelihood and maximized the resulting function:

$$\hat{\beta}_{LASSO} = \text{argmax}_\beta \left(\ell(y, \beta) - \lambda \sum_{k=1}^{K} |\beta_k| \right)$$

and where λ is the hyper-parameter that represents the strength of the LASSO shrinkage. Fig. 12 shows the goodness of fit and beta coefficients as a function of λ.

After this, we applied the classic MLE regression with only the selected regressors to get not penalized β coefficients estimates for the significant regressors:

$$\hat{\beta}_{MLE} = \text{argmax}_\beta \ell(y, \beta)$$

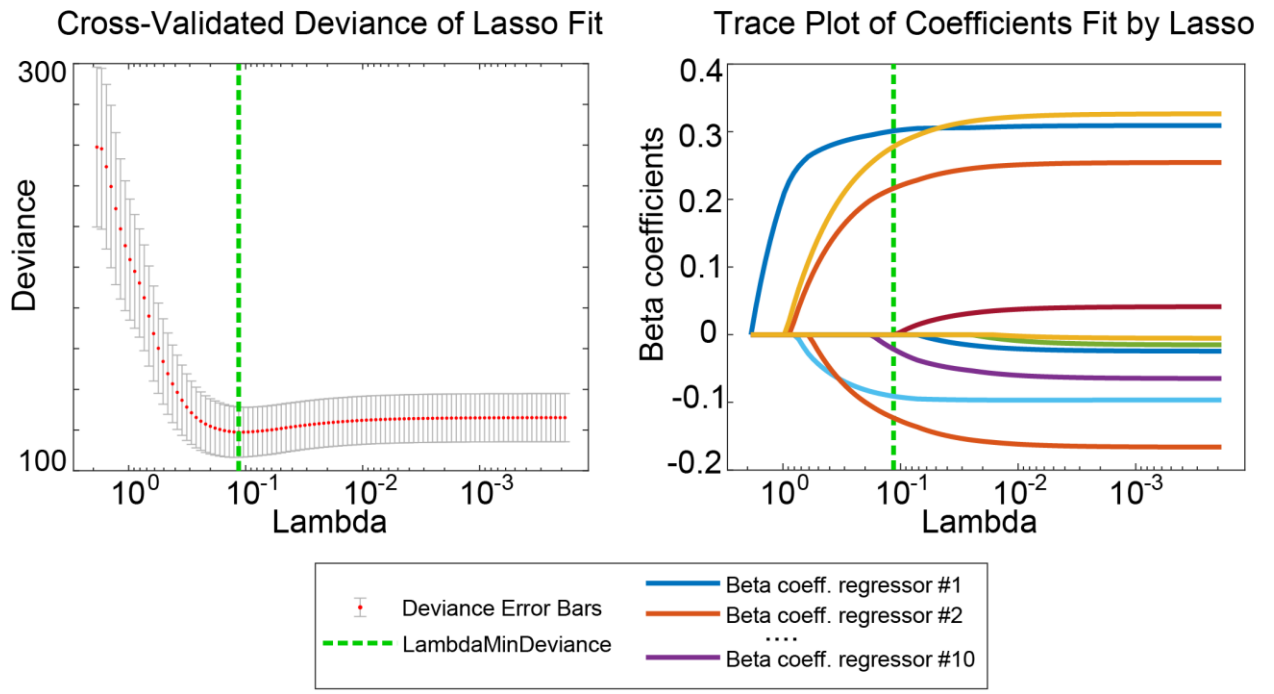

Fig. 12. Example of feature selection using LASSO optimization method on randomly generated data. Left: Cross-validated deviance of LASSO fit models (a measure of the goodness-of-fit) as a function of the shrinking parameter lambda (l). The green dashed line corresponds to the lambda that produce the minimum deviance. Lower lambdas (on the right of the green line) produce a model with too many parameters that suffer of overfitting. Higher lambdas (on the left of the green line) tend to shrink too much the model removing important regressors. Right: Beta coefficients fitted by LASSO as a function of l. Each coloured line represents the value of the coefficient corresponding to a regressor in the model. The green dashed line corresponds to the lambda that produce the minimum deviance, thus the optimal beta coefficients. Lower lambdas (on the right of the green line) produce a model that retains more features (fewer beta coefficients have a 0 estimate). With higher lambdas (on the left of the green line) important features are removed from the model, greatly worsening the fit. Adapted from Vaccari et al., 2021.

3.4 Data pre-processing

We aligned data on the release of home button, then we considered neural activity and eye tracks for all neurons for all trials from -3000 ms to +1720 ms. Cropping trials in this way allowed us to capture the last part of free epoch and the beginning of fixation for every trial; after the release of home button, we captured the whole hold epoch and the returning of arm to the resting position for most of trials. We then binned spiking activity at 40 ms calculating the number of spikes in each bin. We chose this binning interval because we wanted to focus the influence of each regressor on cell activity expressed as its firing rate, rather than predict each spike precisely and direct the attention on spiking mechanics.

For each bin, we calculate the averaged gaze position along x and y coordinates for the two eyes (each 40 ms bin contains 4 points of the raw eye track sampled at 10 ms). We averaged x-position for the two eyes (R_x, L_x)

and y-position for the two eyes ($\mathrm{R_y}, \mathrm{L_y}$), getting a couple of values that indicates for each bin real gaze direction (version and elevation).

$$VERSION = \frac{\mathrm{R_x} + \mathrm{L_x}}{2};\ ELEVATION = \frac{\mathrm{R_y} + \mathrm{L_y}}{2}$$

We also got horizontal vergence for each bin applying the formula:

$$\mathrm{VERGENCE} = L_x - R_x$$

3.4.1 Extrinsic regressors

As gaze modulations are not linear (Breveglieri et al., 2012; Galletti et al., 1995), in order to capture the responses' non-linearity with our model, we discretized the space in front of the monkey. This allowed us to assign a beta coefficient for each spatial volume we considered and allowed to take into account both linear and non-linear gaze modulations with a unique model, approximating neural activity within each volume. First, considering that the reaching targets are in a central frontal position and the animal has to fix them for most part of the trial, we focused on this subregion of the space. We considered the position of the central nearest target as the origin of our x-y (version-elevation) coordinates system. Then we discretized the space in a 15° wide 2D grid that spanned from -22,5° (left side) up to 22,5° (right side) of version (with targets located at -15°,0°,15°) and from -22,5° (bottom) to 22,5° (up) of elevation; we divided the remaining space outside the grid in 4 quadrants (top-right, bottom-right and so on). Note that, since the targets were located at the eye level, elevation during all the fixations was ideally always 0°. For this reason, variations along the vertical coordinate happened most during the free epoch at the beginning of each trial. In addition, we created a 5° wide subdivision based on the vergence obtaining 4 layers of depth (from 20° up to 0°). This subdivision spanned from 20° of vergence (about 8-10 cm of distance from cyclopic eye) up to 0° (infinite distance, with targets located at 17°, 11°, 7°). We chose 20° as maximum limit for the vergence because no object or point of interest for the monkey was nearer than 8-10 cm. We considered each volume obtained from this double-discretization as a dummy variable that took value of 1 only when the monkey 'watches in it'. To have a reliable reference level we removed the dummy variable corresponding to the volume with coordinates (-7,5)°-7,5° (version) x (-7,5)°-7,5° (elevation) 15°-10° (vergence). In this manner we obtained 51 dummy variables ((9 squares in the 2D grid + 4 quadrants) x 4 layers of vergence – 1) indicating for each bin where the animal was looking. We considered them as the EYE POSITION block of regressors of our model.
Then, to compute x,y eye movement velocity, for each bin, for each eye, we subtracted the initial position from the final position of raw eye track , then we divided this angular variation for bin width (40 ms) and averaged the values of the two eyes. Thus, we obtained an average of gaze movement velocity in that

particular bin (°/ms) (x>0, rightward movements; for y>0, upward movements). We normalized it for its highest value across all condition and all trial. In order to take into account actual saccadic neural activity, but also post- and pre-saccadic activity (Kutz et al., 2003), we built several pairs of vectors applying this procedure to eye tracks at bin t, but also to eye tracks at bin t-1, t-2 ... t+1, t+2, … t+n, spanning for the 4 previous and following bins. In this way we fed the model with information on eye movements going from -160 ms up to +160 ms around each bin. We used these vectors as the EYE SPEED/DIR block of regressors of our model.

We built other regressors to take into account the main behavioural epochs of the task. We chose the following epochs: POSTSACC (from fixation start to 500ms after it), DELAY (from target onset to go signal), PREP (from 500ms before go signal to go signal itself), PREMOV (from 200ms before home button release to home button release itself, if more than 200 ms passed after go signal; otherwise, from go signal to home button release) , MOV (from home button release to target touch), HOLD (from target touch to led colour switch), PREMOV2 (from 200ms before target release to target release itself, if more than 200 ms passed after go signal; otherwise, from led colour switch to target release), MOV2 (from target release to Home button pression).

Each of these blocks of regressors contained 9 dummy variables (1 for each target). The first dummy variable for MOV, for example, took the value of 1 in bins in which the animal was moving the arm toward first position in the space and it took 0 in all other bins; the second dummy variable, was 1 for movements toward second targets and so on. We added to the blocks of PREMOV and PREMOV2 regressors a variable containing the reaction time for each trial (normalized on the maximum across all trials and all conditions). We added to the blocks of MOV and MOV2 regressors a variable containing the average movement velocity calculated as the ratio between the distance home button-target and the movement time (normalized on the maximum across all trials and all conditions).

EYE POSITION, EYE SPEED/DIR, POSTSACC, DELAY, PREP, PREMOV, MOV, HOLD, PREMOV2, MOV2 were our blocks of extrinsic regressors.

3.4.2 Intrinsic regressors

We added to the model 5 independent variables providing information about spike history grouped in the block of intrinsic regressors. The first one associated each bin t to spike count at bin t-1, the second one associated each bin t to spike count at bin t-2 and so on. Past spike count had been normalized for his maximum value across all trials and all conditions. In this way, we provided to the model information about the neural activity in the previous 200 ms. In the context of GLMs, it is common to give the model information about other cells' activity in order to take into account cross correlations within the population of neurons (Truccolo et al., 2010). In our case, as our recordings were performed with single electrodes and not

simultaneously, we exclude the possibility of crosstalk between neurons of our population, and we did not provide any information about other cells' activity.

3.5 Fitting procedures

With data consisting of the spike count (dependent variable) and all the vectors of regressors (independent variables), for each cell independently we fitted different Generalized Linear Models following a double-step procedure. Note that our dataset consisted of more than 10^4 datapoints for each cell (118 bins for each trial, 10 trials for target, 9 targets), enough to handle the $\simeq$150 variables we had with a good confidence interval. In the first step, to make a selection of the regressors and retain only the important on cell neural activity, we fitted a GLM with all the available regressors applying the LASSO regularization. This regularization has the property to shrink the unimportant regressions coefficients to zero, so these features can be removed from the model. During this first phase, we performed a 10-fold automatic cross-validation (option 'CV' in *lassoglm* Matlab function that random datapoints to one out of 10 subsets of roughly equal size) to choose the value of λ (see equation 4) that minimizes the deviance of the model. This step allowed us to exclude from the subsequent phase the regressors that got a regression coefficient equal to zero.

In the second step, we fitted different classic GLMs with Poisson distribution using the remaining selected features, grouped in blocks (see Extrinsic Regressors) We performed a leave-one-out cross-validation (training on 9 randomly chosen trials for each target and validating the model on the left-out 1). We repeated this cross-validation procedure 10 times for each model for each cell.

Note that each subset contained $\simeq$9500 datapoints for training and $\simeq$1000 points for testing. Predicted firing rate and the other statistics reported are computed on the test sets.

For each cell, we fitted several models: a ''complete'' one using all the regressor blocks, 10 ''nested'' models excluding from the complete model a different extrinsic block of regressors at a time, an ''intrinsic only'' model removing all the extrinsic regressor blocks, an ''extrinsic only'' model removing all the intrinsic regressor blocks and finally a ''null'' model with only the intercept that represented the ground zero goodness of fit. All the analyses and results reported in this paper were relative to these non-LASSO-regularized models. This choice was due to two reasons: to treat at the end of the fitting procedure beta coefficients not penalized by the LASSO penalty term and, most important, to avoid the exclusion of a different number of features when fitting the different nested models. In fact, for the model comparison it was fundamental to remove the regressors in a controlled way starting from the complete model, whereas the LASSO regularization, if used for the nested models, it may have resulted in an additional removal of regressors in an automatic (thus not controlled) manner.

Fig. 13 shows the workflow of the data analyzed for the present study, from collection during the experimental recording to model fitting and beta coefficient estimation.

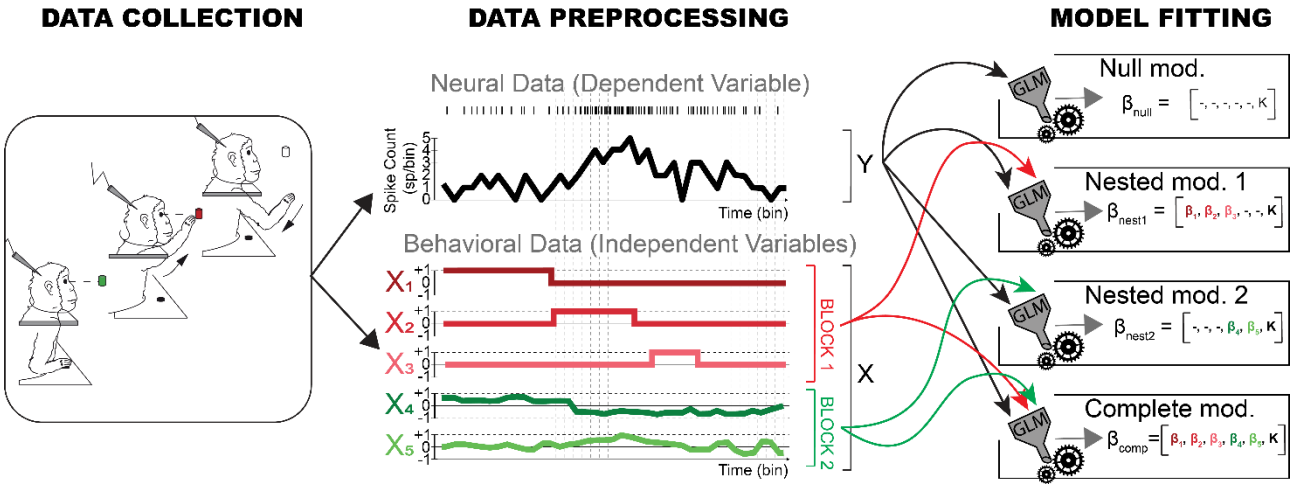

Fig. 13. Workflow schematic representation. Left: experimental session during which neural data are recorded simultaneously to behavioural data (DATA COLLECTION). Center: data are pre-processed (binning, normalization) to build the vector of spike-count Y and the regressor matrix X; regressors can be in form of dummy (e.g., X1-3 in the figure) or continuous (e.g., X4-5) variables and, regardless of their type, variables with similar meaning can be grouped together (e.g., in the scheme, X1-3 and X4-5 are grouped in block1 and block2, respectively; DATA PREPROCESSING). Right: several models are fitted with the data (the null model based only on the neural data, the nested models with certain block of regressors removed and the complete model) and beta coefficients are estimated. Note that in the scheme, the LASSO feature selection is omitted for the sake of simplicity (MODEL FITTING). Adapted from Vaccari et al., 2021.

3.6 Units selection and analysis of fitted models

3.6.1 Single cell level

We tried to select task-related cells to reduce noise in our population. For this purpose, we computed the mean firing rate in each epoch of interest (8, see 'Extrinsic regressors' for more details) in each trial and we performed one-way ANOVA (factor: epoch; levels: 8). All units resulted significantly modulated in at least one epoch (ANOVA $p<0.05$ for every unit). Thus, we proceeded with a cell selection based on the fitting of our model (see below). To quantify our complete model goodness of fit and make it easy to interpret, we used a pseudo-R^2. McFadden's pseudo-R^2, for Poisson GLMs, can be calculated (Cameron and Windmeijer, 1997) starting from the log-likelihood of the complete fitted (ℓ_{complete}) and null (ℓ_{null}) models:

$$R^2_{\text{pseudo}} = 1 - \frac{\ell_{\text{complete}}}{\ell_{\text{null}}}$$

The log-likelihood of the null model (a model with only the intercept) represented the ground zero value and, by definition, it is independent from every regressor. Note that McFadden's pseudo-R^2 can be interpreted as the more common R^2 in ordinary linear regression, ranging from 0 (extremely poor fit) to 1 (perfect fit), but its values tend to be considerably lower (values of 0.2 to 0.4 are considered excellent fit). When calculated

on test datasets (data never seen by the model during the fitting), pseudo-R^2 values are even lower. We selected those units that reached at least a pseudo-R^2 relative to the complete model of 0.05 to discard the noisier part of population or neurons for which our model failed to capture neural activity modulations (Goodman et al., 2019; Paninski et al., 2004a). To analyze the nested models (see 'Fitting procedures') and to get a score associated with the importance on neural activity of the information contained in every block of regressors, we proceeded as follows. First at all, we calculated a relative pseudo-R^2 as:

$$R^2_{\text{relativepseudo}} = \frac{\ell_{\text{nested}} - \ell_{\text{null}}}{\ell_{complete} - \ell_{\text{null}}}$$

where ℓ_{nested} is the log-likelihood of the nested model. This value compares the log-likelihood (i.e.,the goodness-of-fit) of each nested model with the one of the complete model (and of the null model). Then, for a higher interpretability, we converted the relative pseudo-R^2 in a weight (w-value) = 1 - relative pseudo-R^2. We used this as a score directly associated with the importance of groups of variables on the complete model. The idea behind this metric is that to build each nested model, we removed from the complete model a block of regressors, leading a worsening in the fitting. Whether a block of regressors contained important information for the model, its removal causes a great worsening of the fit, the relative pseudo-R^2 will decrease (towards 0) and the w-value will increase (towards 1). Vice versa, whether a regressors' block had little influence on the complete model, its removal will cause a little worsening of the fit, an increase (towards 1) in the relative pseudo-R^2 resulting finally in a little w-value (towards 0). From these computations, we obtained a set of w-values (1 for each extrinsic block of regressors, 10 in total; 1 for the extrinsic-only model that corresponds to the removal of the SPIKE HISTORY block and 1 for the intrinsic-only model) for each selected cell that allowed us to evaluate the influence of the different parts of our model on neural activity. It is worthy to remark that the w-values express the goodness of fit of the nested model in comparison with the complete one. Thus, a neuron can have a larger w-value for a block of regressors than another having less deviance explained by that block in absolute. Furthermore, they do not carry necessarily information about the spatial tuning of the cell. We used the 10 w-values of the extrinsic blocks to build the 'functional fingerprint' for each unit. This fingerprint shows how the cell is sensitive to the various external factors considered by our model.

3.6.2 Population level: extrinsic blocks of regressors

We further analyzed the extrinsic blocks of regressor across the population. We checked consistency of the results in the animals comparing the distribution of median values for all the blocks of regressors between the two animals (two-samples Kolmogorov-Smirnov test, $p<0.05$). To find the elbow of the w-values

distributions , we first split the curves in two parts and then fitted one line for each part. We repeated this procedure to find the dividing point (the elbow) that minimize the sum of fitting errors.

We used PCA to reduce dimensions of data and to visualize them in a 3D space (the first 3 PCs). To look for a clustering in the population based on type of modulations (for example visual cells, motor cells, visuomotor cells modulated by gaze-position and movement, but not by hold epoch…), we then applied K-means clustering algorithm on the raw w-values (not manipulated with PCA). This algorithm needs the number of clusters to seek in input. So, to find out the optimal one, we tried with three of the most common procedures: elbow, average silhouette and Gap statistic method. Furthermore, we also tried a hierarchical clustering of the w-values. All the techniques we employed failed in finding different clusters in the data. To highlight the continuity in the modulations and the mixed selectivity characteristic of area V6A, we colored the dots in PCA representation according to the w-values of the three most important extrinsic blocks of regressors.

In order to study the selectivity for one of the extrinsic blocks of regressors (or the lack of it, i.e.,mixed selectivity), we chose to calculate the number of important blocks on each unit spiking activity. For each cell, we summed all its extrinsic w-values. Then, we iteratively added together in descending order the extrinsic w-values up to reach 85 % of the total sum. The blocks required to achieve this value have been identified as important on that cell spiking activity. The obtained number can range from 1 (cell selective for only one feature) to 9 (cell equally selective for all the 10 features).

3.6.3 Spatial and temporal correlations

To study the spatial and temporal evolution of the population encoding, we performed a correlation analysis on the beta coefficients resulting from the complete models (Zhang et al. 2017). For each cell, we averaged the beta coefficients resulting from the 10 cross-validation training subsets. We then built a population vector with the beta coefficients of each cell for every spatial position and every epoch. We evaluated the correlations between vectors of beta coefficients of each pair of positions within each epoch separately (spatial correlations) and between vectors of beta coefficients of each position in subsequent epochs (temporal correlations) with the Spearman's rank correlation coefficient ($R_{Spearman}$). This coefficient does not assess linearity between the variables, but only monotonic relationships and, exploiting the rank, it is less sensitive to the outliers. We used a linear regression to assess the dependence (r) of strength of correlations ($R_{Spearman}$) on the spatial distance between two target positions (measured directly on the reaching panel, fig. 11B). Finally, we averaged both the spatial and the temporal correlations to have results easier to interpret.

3.6.4 Spike history influence

The influence of the intrinsic part of the model on the fitting has been evaluated plotting the w-values for the intrinsic part of the model and for the extrinsic part (calculated on the extrinsic-only and intrinsic-only

models, respectively) in a scatterplot where each dot represents a cell. We extracted from the complete model the 5 beta coefficients relative to different lags of the spike history for each cell and we ran on them a K-means clustering algorithm with 100 replicates with different random initial centroids and choosing the result with the lowest sum of point-to-centroid distances. We tested whether there was an association between the 2 sub-groups and the 2 animals with a chi-squared test (n° of M1 units in one sub-group / total n° of M1 units vs n° of M2 units in the same sub-group / total n° of M2 units). To represent these data, we used PCA to reduce their dimensionality projecting the cells and their grouping in the plane of the first 2 PCs. We averaged the 5 beta coefficients within each sub-group and tested if distributions of the 5 beta coefficients were different between the sub-groups (t-test, $p<0.05$).

4 RESULTS

Our dataset consisted of cells that were recorded for 10 correct trials for each of the 9 targets (N=181; 64 from M1, 117 from M2; see fig. 14 for the recording sites).

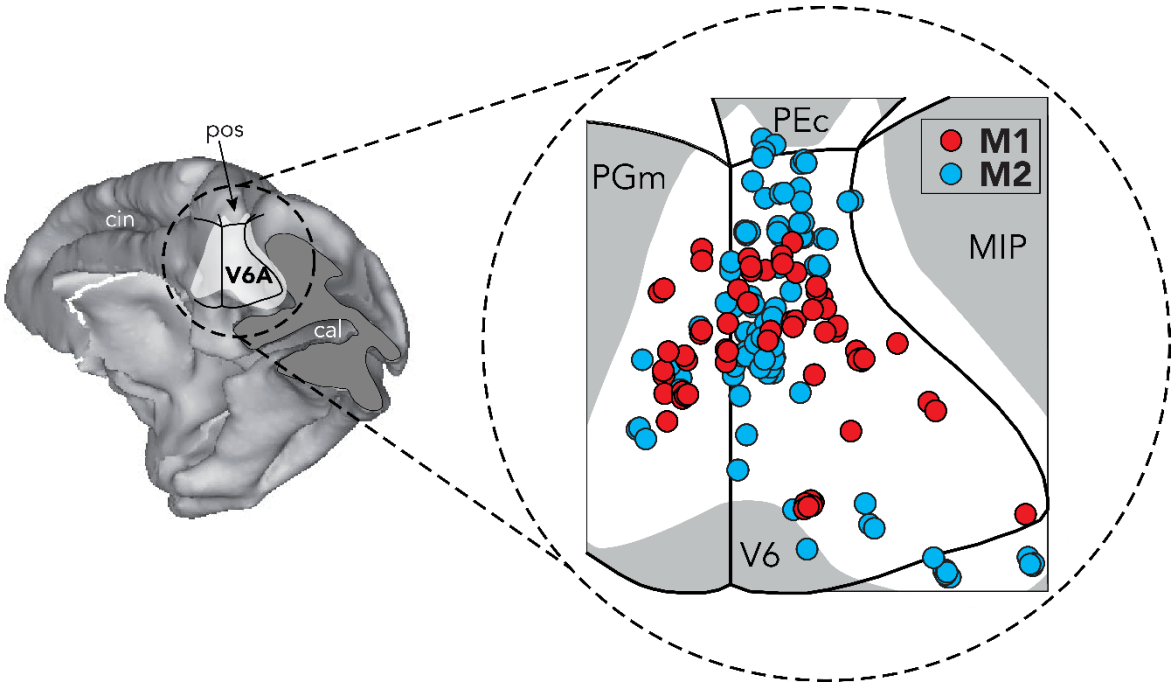

Fig. 14. Recording sites in the two animals. On the left, posteromedial view of 3D-reconstructed macaque brain. The posterior part of the occipital lobe was cut off to visualize the entire extent of the anterior bank of parieto-occipital sulcus. Superimposed, a flattened map of the caudal part of the SPL. The level of the cut is shown in grey. On the right, the 2D map of caudal SPL with the locations of recorded neurons in area V6A for the 2 monkeys (red M1, blue M2). Abbreviations: cal, calcarine sulcus; pos, parieto-occipital sulcus; cin, cingulate sulcus.

To reduce sources of noise we performed a 1-way ANOVA (factor: epoch; levels: 8;) on mean firing rates within epochs of interest (for more details see Methods) to identify task-related cells. The entire population resulted modulated for at least one epoch with no exceptions. Furthermore, we selected the cells according to the goodness-of-fit of our model (see below). Spikes were counted in 40 ms bins and all trials were concatenated tip to tail in a unique vector for each cell that represented the dependent variable). In the GLM context a dependent variable is explained with a combination of independent variables called 'regressors' or 'features' in this paper (fig. 13). Each independent variable was a vector of the same length of the dependent variable. The regressors were organized in blocks. EYE POSITION block contained information about the average gaze position discretized in a 3D grid for each bin (see Methods); EYE SPEED/DIR block contained information about the velocity and the direction of eye movements; POSTSACC, FIX, PREP, PREMOV, MOV, HOLD, PREMOV2, MOV2 were blocks that contained spatio-temporal information about the sequence of behavioral epochs occurring along the task (see fig. 11B for the temporal sequence of the task and Methods

for details). We refer to these blocks of regressors as 'extrinsic'. The SPIKEHISTORY block contained information about firing activity of the neuron in the previous 200ms. We refer to it as 'intrinsic' block. For each cell, we first selected the most relevant regressors with LASSO regularization technique. This first step led us to retain on average 90 ± 20 (standard deviation) regressors over ≃150 across the entire population (non-zero beta coefficients estimated by LASSO). Then, for each cell, we built several Poisson GLMs: a complete model that included all the selected regressors; 10 nested models in which we removed each time a different block of extrinsic regressors; 1 nested model removing the intrinsic block of regressors (extrinsic-only model); 1 nested model removing all the extrinsic blocks of regressors (intrinsic-only model). All the models were cross-validated and reported results are relative to the test datasets never seen by the no-LASSO-regularized models during the fitting (see Methods). To discard the units for which the model failed to capture neural modulations, we chose to select only the cells which pseudo-R^2 of the complete model reached at least 0.05, a criterion used in literature (Goodman el a., 2019; see Methods). As a result, 50/64 (78%) M1 units and 65/117 (56%) M2 units met this criterion and were retained for further analyses. For selected cells, pseudo-R^2 was 0.102 [0.073, 0.147] (median [25^{th}, 75^{th} percentile]). To evaluate the influence of the different parts of our model (blocks of regressors) on neural activity, we first calculated for each nested model a relative pseudo-R^2 that compared its goodness-of-fit with the complete model goodness-of-fit. We then adopted a metric that we called 'w-value' (1 – relative pseudo-R^2) directly proportional to the weight (i.e.,the importance) of each block of regressors on the fitting of the complete. Each w-value ranged from 0 (no influence of the removed block of regressors on spiking activity) to 1 (greatest influence of the block of regressors; See Methods for further details). The set of the 10 extrinsic w-values functionally qualifies each cell and represents what we called 'functional fingerprint'.

4.1 Analysis at single cell level

Fig. 15 shows data of two different example neurons (A, B). The column plots in the bottom part of the figure represent the 'functional fingerprint' of cells shown in A and B, respectively. The first neuron (fig. 15A) showed strong changes in the discharge during the PREMOV and MOV epochs (light and dark blue, fig. 15A top) while during the other time epochs little or no effects were observed. In fact, the firing rate (dashed line) suddenly increased in PREMOV (just before the onset of arm movement) and remained high throughout the whole movement phase. A few motor-related parameters (linked to PREMOV and MOV epochs) explained most of cell modulation (highest columns, fig. 15A bottom). In the column plot, we marked with asterisks the blocks that resulted the most important to explain the neural activity from our analysis (see Methods).

The neuron reported in fig. 15B had more complex modulations. It showed a clear preference for far positions and a peak in the activity when the animal reached them. Indeed, starting from the beginning of fixation, cell discharge was remarkably higher for far positions than for the others. Moreover, for far positions, it increased

just before the movement onset (PREMOV) and reached a peak after it (MOV). On the contrary, for intermediate positions the neural activity was generally low and even lower for near positions. Interestingly, during the epochs of major activity for far positions (PREMOV and MOV), the neuron resulted almost completely inhibited when the animal gazed and reached near positions. The 'functional fingerprint' (fig. 15B bottom) shows the mixed selectivity of this cell, with 6 regressor blocks that significantly influence cell discharge (mainly PREMOV, MOV, HOLD, but also EYE POSITION, PREP and MOV2).

It is worth noting that the 'functional fingerprint' does not provide information about the spatial tuning of the unit, because it accounts for the overall influence of different parameters upon cell discharge (averaging the effect of parameters in different spatial positions) rather than accounting for changes in cell discharge according to the spatial position. Indeed, the functional fingerprint of cell in fig. 15A is much more selective (only a few parameters do influence cell discharge) than the one of cell in fig. 15B, even if the spatial selectivity of cell in fig. 15B is strikingly higher than the spatial selectivity of cell in fig. 15A.

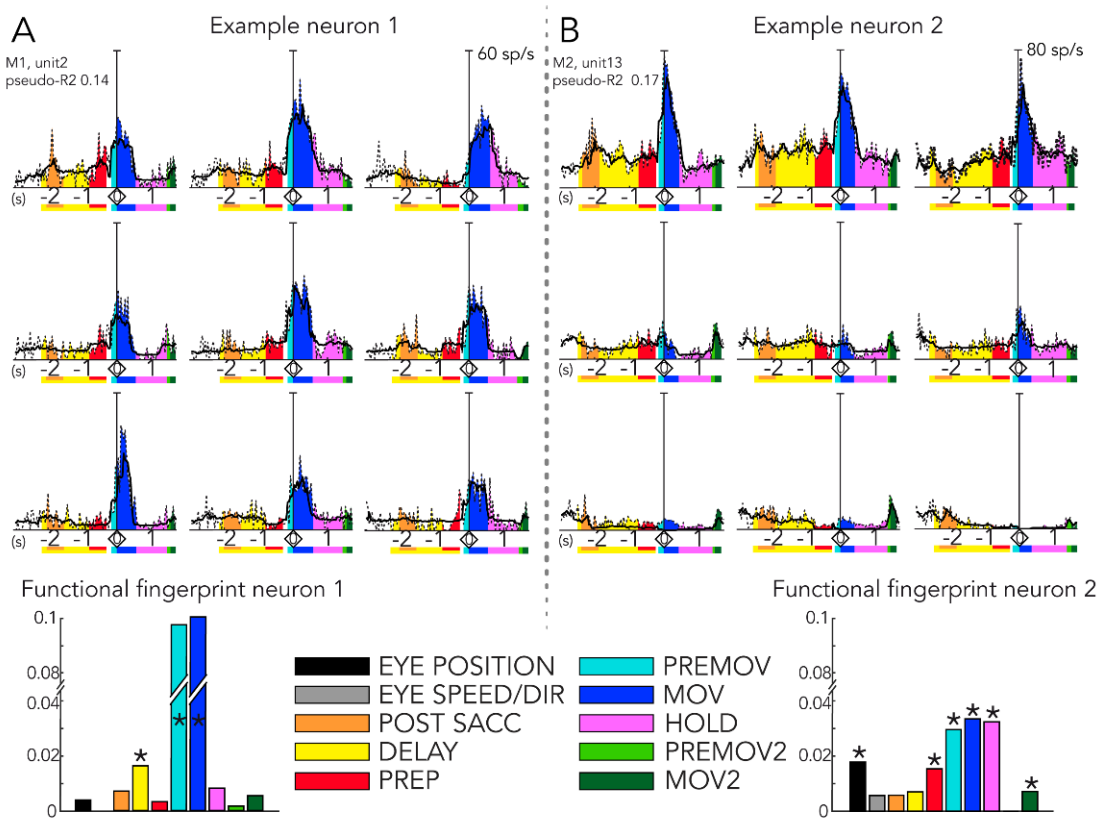

Fig. 15. Examples of single-cell activity. (A) Neuron showing a marked selectivity for somato-motor components of the task; (B) a neuron with a mixed selectivity for several parameters. (Top) Plots are arranged according to the spatial position of targets over the panel (rows for different depths; columns for different directions, see fig. 1B). Recorded (mOBS, dashed line) and predicted (mEST, black continuous line) averaged firing rates (bin width: 40ms). In each plot, data relative to the 10-fold validation sets are averaged across trials for each of the nine targets and aligned on movement onset (time ''<0>''). Colours represent the epochs considered in the model. (Bottom) Bars show the weights (w-values) of the 10 extrinsic blocks of regressors (the ''functional fingerprints'' of the neurons) on the neural activity. Asterisks indicate most important w-values for each cell (their sum reaches at least 85% of the sum of all w-values of the cell, see Methods). Adapted from Diomedi et al., 2020.

4.2 Population analysis

To understand how the functional properties were encoded in the V6A population, we further analyzed the results obtained cell-by-cell at population level. As described above, for each recorded neuron, we calculated 10 w-values, one for each of the extrinsic blocks of regressors. We first checked whether these w-values across the population were consistent between the two animals (fig. 16A, B; medians and intervals in Table 1). Despite some differences for single blocks (such as PREMOV that was higher in M1 than M2 or MOV and HOLD values that were slightly lower), the overall distribution of the median values of each block of regressors was consistent (Kolmogorov-Smirnov test, p=0.6751). Fig. 16A shows that in both animals the extrinsic regressors with higher w-values were EYE POSITION, MOV, and HOLD (median values for M1+M2: 0.018, 0.015 and 0.016 respectively). Data of M1 and M2 pooled together are shown in fig. 17.

The distribution of w-values sorted separately for each block of regressors showed that just a few cells in both animals had very high w-value, while the remaining cells (the large majority) showed gradually descending values (fig. 16B). It is possible to identify an elbow that splits the curve in two parts (see Methods). On average, the dividing point corresponded to the 90 ± 5 % of the population (mean and standard deviation across all blocks and the two animals). In other words, focusing on each regressor, only a few cells (10 %) were well modulated by that parameter while most of the cells (the remaining 90 %) showed mild or low modulations.

Because each cell is described with a unique vector of w-values (functional fingerprint), in order to visualize this multidimensional data and investigate whether a functional structure does exist, we performed a Principal Component Analysis (PCA) on the extrinsic w-values (fig. 16C). No definite clustering of the data emerged from this analysis: the majority of cells were grouped together, with some outlier, sparse units. We tried to apply the most common clustering techniques (such as K-means and hierarchical clustering; see Methods), but any attempts failed to identify a segregation in our data.

To visually check whether there was a trend within the population, we colored in fig. 16C the dots according to cell modulations. For graphical purposes, we chose only the three main blocks of regressors (EYE POSITION, MOV, HOLD). Given the three pure colors associated with each of the three regressors (black, blue and purple respectively, see color code in fig. 16), each neuron (dot) was colored with a mixture of these colors based on its series of w-values (i.e.,with a linear combination of colors weighed with the three w-values). The resulting colors of the outlier cells were similar to three pure ones and thus they were the most selective for these parameters, while the majority of cells showed a combination of the three colors. For instance, the unit of fig. 15A, with high w-values for PREMOV and MOV, is located outside the central cloud of points in fig. 16C (bullseye indicated by filled arrow) and almost purely blue. On the contrary, the unit of fig. 15B is located in the central part of the PCs' space and it is colored according to its 'mixed modulation' nature (fig.

16C, bullseye indicated by empty arrow). The gradual transition from one color to another across the dots is in accordance with the continuum of the w-values distributions (see fig. 16B).

To study cell selectivity for one block of regressors (vs non-selectivity, i.e.,mixed selectivity), beyond the three main ones considered in fig. 16C, we computed how many blocks really matter for explaining the neural activity. Because of the variability both in the distribution and in the absolute values in the functional fingerprints, we adopted an adaptive threshold that took into account the cell total sum of w-values (see Methods). This procedure allowed us to calculate that, on average, each cell was significantly modulated by 4.2 (± 1.3) blocks of regressors (mean and standard deviation). Fig. 16D shows the distribution across the entire population. Units on the left of the histogram were more selective (less parameters were needed to explain neural modulations), while units on the right were characterized by more complex and mixed modulations. In accordance with what already discussed, the example units of fig. 15 fell in opposite parts of the histogram: indeed, the cell of fig. 15A (filled arrow), more selective, with 3 modulating blocks of regressors, is in the left part; the cell of fig. 15B (empty arrow), with 6 modulating blocks, in the right part. As we partially expected, although V6A cells typically showed mixed selectivity, we never observed a 'totally mixed' selectivity (i.e.,cells with 8-9 important blocks).

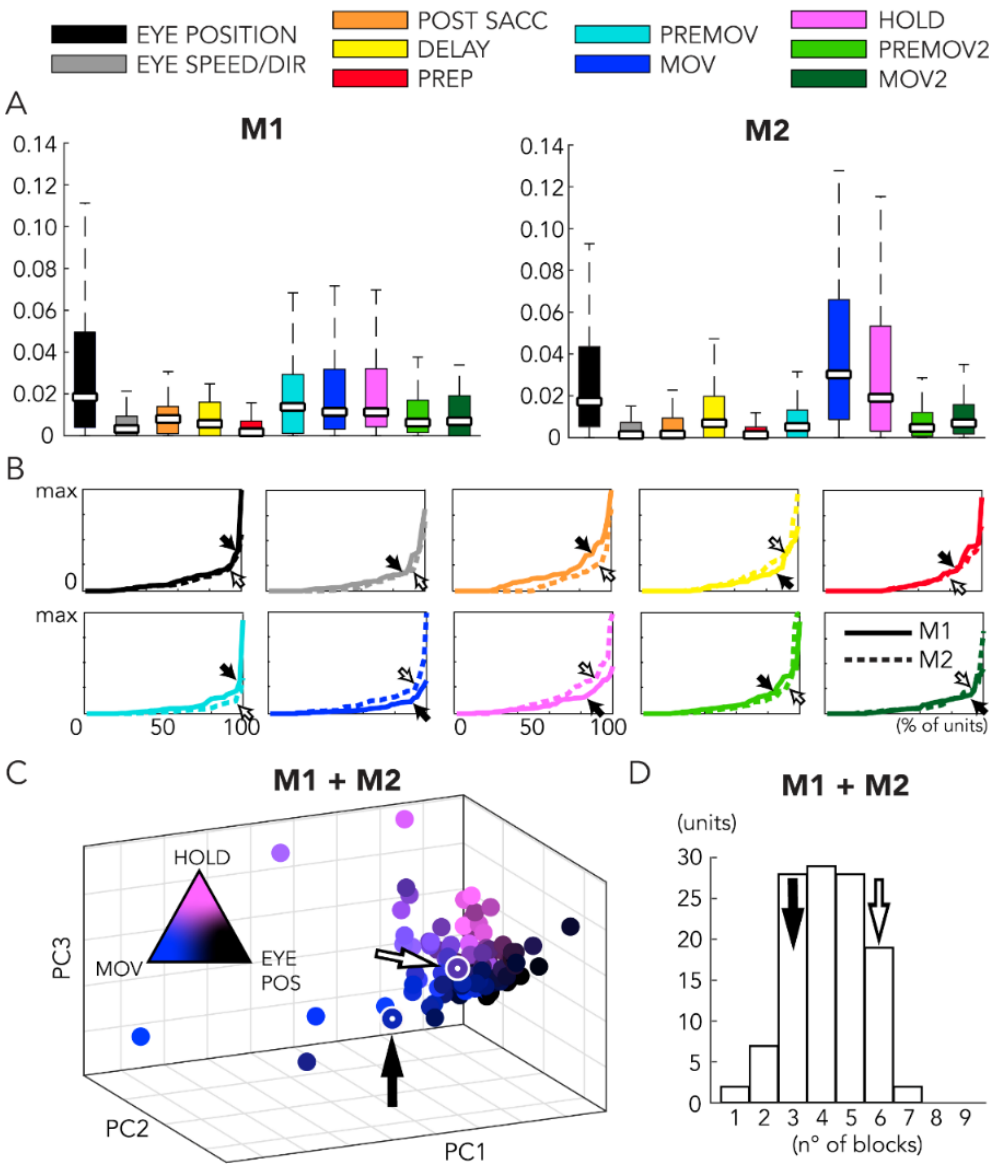

Fig. 16. Extrinsic regressors' weights across the population. A) Box plot of w-values for each block of regressors across the population for the two animals separately. In each box, the central white mark represents the median, while the bottom and top edges of the box indicate the 25th and 75th percentiles, respectively. The whiskers extend to the most extreme data points discarding outliers (Matlab function: boxplot). B) W-values are plotted in ascending order for each block of regressors. Solid and empty arrows indicate the elbow of the curves for M1 and M2, respectively. C) Representation of the neural population (a dot for each cell) using the first 3 principal components (PCs) of the principal component analysis (PCA) performed on the 10 extrinsic w-values. Dots take different combinations of 3 colors according to their w-values for the 3 most important regressor blocks (black for EYE POSITION, blue for MOV, pink for HOLD). Bullseyes indicated by solid and empty arrows represent the example neurons showed in fig. 15A and 15B respectively. D) Histogram showing the minimum number of extrinsic regressors' blocks (w-values) necessary for each cell to reach at least the 85% of its extrinsic w-values total sum (see Methods). Solid and empty arrows indicate where example neurons of fig. 15A and 15B, respectively fall. Adapted from Diomedi et al., 2020.

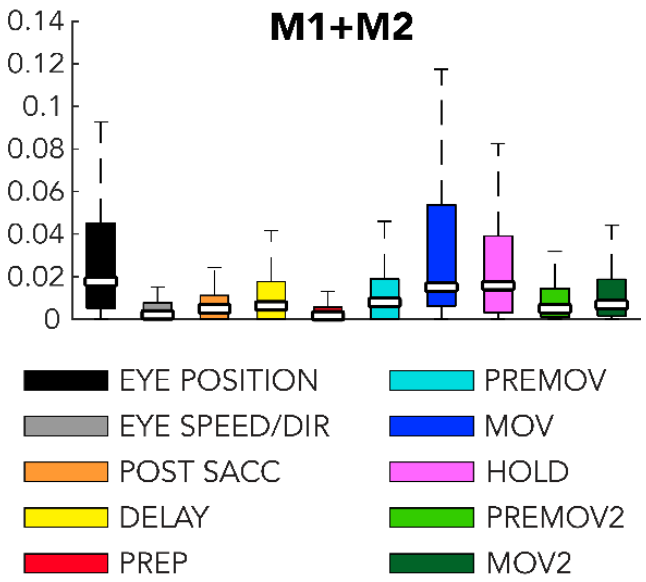

Fig. 17. Extrinsic regressors' influence across the population (two animals' data were pooled together). Box plot of the w-values for each block of regressors across the population obtained merging data from the 2 animals. The same data are reported in Table 1. Adapted from Diomedi et al., 2020.

	EYEPOS	EYESPEED	POSTSACC	DELAY	PREP	PREMOV	MOV	HOLD	PREMOV2	MOV2
M1	'0.018 [0.004 0.050]'	'0.003 [0.0005 0.009]'	'0.008 [0.0008 0.014]'	'0.006 [0 0.016]'	'0.0015 [0 0.007]'	'0.014 [0.001 0.030]'	'0.011 [0.003 0.033]'	'0.011 [0.003 0.032]'	'0.006 [0.001 0.017]'	'0.007 [0.0005 0.019]'
M2	'0.017 [0.005 0.044]'	'0.001 [0 0.007]'	'0.0003 [0 0.009]'	'0.007 [0 0.019]'	'0.001 [0 0.005]'	'0.005 [0 0.013]'	'0.030 [0.008 0.066]'	'0.019 [0.003 0.054]'	'0.004 [0.0005 0.012]'	'0.007 [0.002 0.016]'
M1 + M2	'0.018 [0.004 0.045]'	'0.002 [0 0.008]'	'0.004 [0 0.011]'	'0.005 [0 0.017]'	'0.001 [0 0.005]'	'0.007 [0 0.019]'	'0.015 [0.006 0.054]'	'0.015 [0.003 0.039]'	'0.005 [0.001 0.014]'	'0.007 [0.001 0.018]'

Table 1. 'Median [25-th percentile 75-th percentile]' of the w-values for the M1, M2, M1+M2 relative to every block of regressors, related to fig. 16-17.

4.3 Spatial and temporal correlation

Up to here, we focused on the neural modulations explained by each block of regressors. However, our population analysis based on w-values did not give any direct indications about the spatial tuning while it is known that area V6A is strongly influenced by direction and depth during reaching task (Hadjidimitrakis et al. 2019, 2014; Fattori et al. 2017, 2005; Battaglia-Mayer et al., 2000). To study the dynamics (or the lack of) of the spatial selectivity at population level, we extracted information about changes in the beta coefficients

(i.e.,the modulations captured by the model) performing a correlation analysis, similarly to recent studies (e.g. Zhang et al., 2017). Population activity for each target position and for each epoch can be expressed by a vector of beta coefficients extracted from the GL complete models (one beta for each cell). In the graphs of fig. 18A, B, each node represents a target position. The colors of the edges represent the strength of the correlation between the two beta vectors of two *different positions* within the *same epoch* (fig. 18A) or between the two beta vectors of the *same position* across two *subsequent epochs* (fig. 18B). For a simpler interpretation, these results are averaged and summarized by the plots in fig. 18C, D.

Fig. 18A shows the correlations between two *different positions* within the *same epoch.* The three panels (DELAY, MOV and HOLD) display the three epochs that resulted to be the most important ones after merging the data of the two animals (highest median w-values, see fig. 17 / Table 1). Moreover, for graphical purposes, we split all the pairwise correlations (36 edges) in two graphs for each epoch based on the physical distance between the linked nodes (top: short distance <= 10 cm, bottom: long distance > 10 cm). We found differences among these epochs: HOLD was characterized by correlation coefficients generally higher than the others (0.58 ± 0.12, mean ± standard deviation); MOV had lower values (0.14 ± 0.25); DELAY showed an intermediate strength in correlation (0.33 ± 0.15). Thus, the strength of spatial correlations (i.e.,how similar population activity is between two different targets) varied along the trial. These fluctuations are shown in fig. 18C. In the figure, the plot represents the averaged correlation for all epochs. The peak of the plot corresponds to HOLD epoch, confirming what we already observed in fig. 18A (higher correlations). It is noteworthy that, within each epoch, there are huge differences in the strength of correlations depending on the physical distance of the two linked nodes (targets). Indeed, for all the three epochs in fig. 18A, within the same panel (epoch), bottom graphs (higher distances) show lower correlations than the upper ones (lower distances). This decrease in correlations strength with the increase of distance is highly significant (linear correlation, r = [-0.78; -0.91; -0.70], $p \simeq [10^{-8}; 10^{-14}; 10^{-6}]$ for DELAY, MOV and HOLD respectively; we observed the same effect in the remaining epochs, data not shown).

To study the changes in regression coefficients in a spatial-independent manner, we also correlated the two beta vectors of the *same position* across two *subsequent epochs.* This allowed to study the temporal evolution of the population encoding (fig. 18B). The figure displays only the epochs that represent the central part of the task, while fig. 18D shows the mean correlation values along the whole task. High correlation values indicate a stable pattern of population activity between two epochs (i.e.,the neural activity for the same target is similar across the two epochs). At the beginning of the trial, the correlations were negative or near to 0 while they reached a sort of plateau with higher values as the task progressed (see fig. 18D).

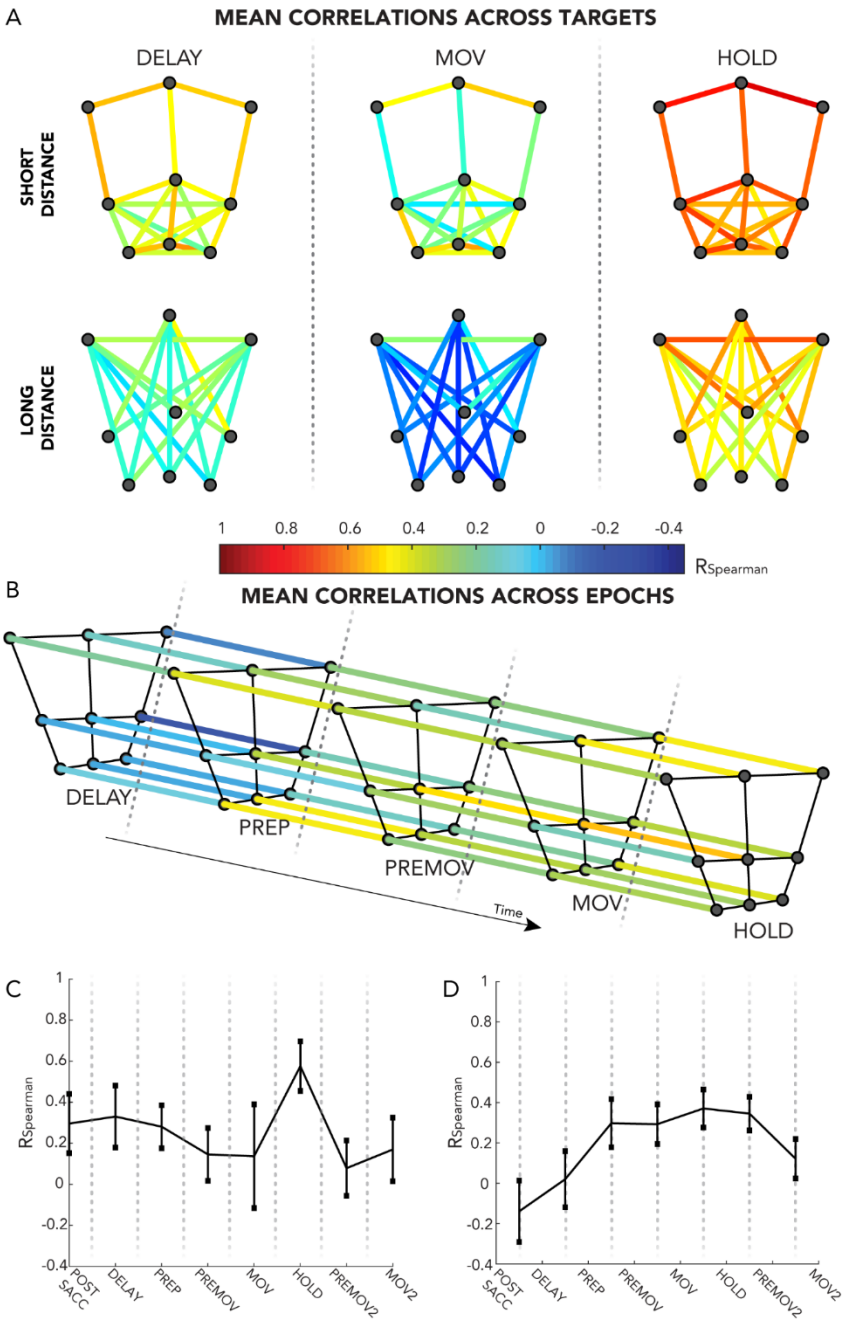

Fig. 18. Spatial and temporal correlations between beta coefficients. A) Correlations between beta coefficients of the population of different target positions within the same epoch. In the graphs, nodes represent the 9 targets (see fig. 11A). Edges represent the correlation coefficient between beta coefficients of two different positions. Three panels show the three main epochs (DELAY, MOV and HOLD). Top: edges link targets at short distance, bottom: edges for targets at long distances. Note that target positions are altered for graphical purposes. For a general trend across the task, see C) and for details about the other epochs see Methods. B) Correlations between beta coefficients of the population of the same target across subsequent epochs. In the graphs, nodes represent the 9 targets (see fig. 11A). Edges represent the correlation coefficient between beta coefficients of two different epochs. The figure shows only the epochs of the central part of the task. For a general trend across the task, see D). C) Mean correlation between beta coefficients of different target positions within the same epoch. Same data as in A), but all pairwise correlations between targets are averaged. Error bars indicate the standard deviation. D) Mean correlation between beta coefficients of the same target across subsequent epochs. Same data as in B), but pairwise correlations between epochs are averaged. Error bars indicate the standard deviation. Adapted from Diomedi et al., 2020.

4.4 Spike history influence

Until now, the analyses were focused on the extrinsic regressors. To study also the contribution on the fitting of the intrinsic part of the model, we compared the intrinsic w-value with the extrinsic w-value for each cell (fig. 19A). The scatterplot shows that a significant number of neurons (71/115, 62%) lied above the diagonal, that is the w-value for the intrinsic part of the model was higher than the one for the extrinsic part. It is remarkable that the spike history, represented in the model by only 5 regressors over a total of $\simeq$150, predicted better the spiking activity than all the other variables in about the 60% of cells. This is in accordance with the complex associative nature of area V6A (see Discussion). Since the regressors have been normalized in the range [0, 1] independently for each cell before the fitting, we extracted from the complete models the 5 beta coefficients relative to the spike history (1 for each time lags, see Methods) and directly compared them across the population (fig. 19B). Positive beta coefficients meant an excitatory effect of the spike history on the spiking activity, while negative values represented inhibition. The overall influence on neural activity of -200ms and -160ms time lags were low. More recent spiking events had on average higher effect. The most recent time lag (-40ms) showed a broad distribution ranging from inhibition to the strongest excitatory effects. Regarding the beta distributions, they were continuous, suggesting a gradual transition from more excited to less modulated (or inhibited) cells. To highlight the main trends within the neural data, we ran a K-means clustering algorithm with 100 replicates to find a stable partition of the population into two sub-groups (i.e., a local minimum of the function, see Methods). We tried also to look for a greater number of clusters, but the three common techniques (elbow, gap statistics, silhouette) we used to choose the optimal number failed to converge. We performed a PCA to reduce the dimensionality of our datapoints from 5-dimesional space (i.e.,5 spike history betas for each cell) to a 2-dimensional space (i.e., the first 2 PCs that explained the 86% of the variance) in order to represent the sub-groups in a Cartesian plane (fig. 19C). The two sub-groups included 70/115 (61%) and 45/115 (39%) units, respectively.

Note that, even if the clustering algorithm had been run on the original betas, the two sub-groups were almost perfectly separated according to the value of the first PC. From an inspection of PCA loadings, it turned out that most information that this PC carried was related to the -40 ms lag beta (61% of the first PC total loadings). These findings were in accordance with the higher variance of the most recent time lag beta coefficients with respect to the other betas (fig. 19B), leading them to drive the PCA and the clustering. We did not find any correlation between the sub-groups and the two animals (chi-squared test on the ratios, p=0.61). Conversely, we did find that, whereas the first sub-group was equally distributed with about the 50% of cells above and under the diagonal of the scatter plot in Fig., 19A, the units of the second sub-group lied mainly above the diagonal (75%). This higher influence of spike history on the model for this sub-group was coherent with its higher beta coefficients (see below).

Fig. 19D shows means and standard deviations for the 5 spike history betas within each sub-group. The regression coefficients distributions were overlapping and no-significantly different (t-test, p>0.05) for -200,

-160 and -120 ms time lag. They were significantly different (t-test, p<0.05) for the -80 ms time lag, even if the error bars still partially overlapped and they finally differed (t-test, p<0.05) and did not overlap for the most recent (-40 ms) time lag, the one that drove the clustering. To sum up, while the first sub-group had a mild excitatory modulation for the recent spike history (-120, -80 and -40ms) that decreased for the previous time lags (-200 and -160 ms), the second sub-group had a higher excitatory effect that increased almost linearly for the more recent time lags. Note that inhibitory effects (negative betas in the fig. 19B, especially for -40 ms lag) sporadically observed for some cells did not constitute a significant trend in the population. Indeed, they almost completely disappeared computing the standard deviation (as in fig. 19D) instead of considering the boxplots (as in fig. 19B).

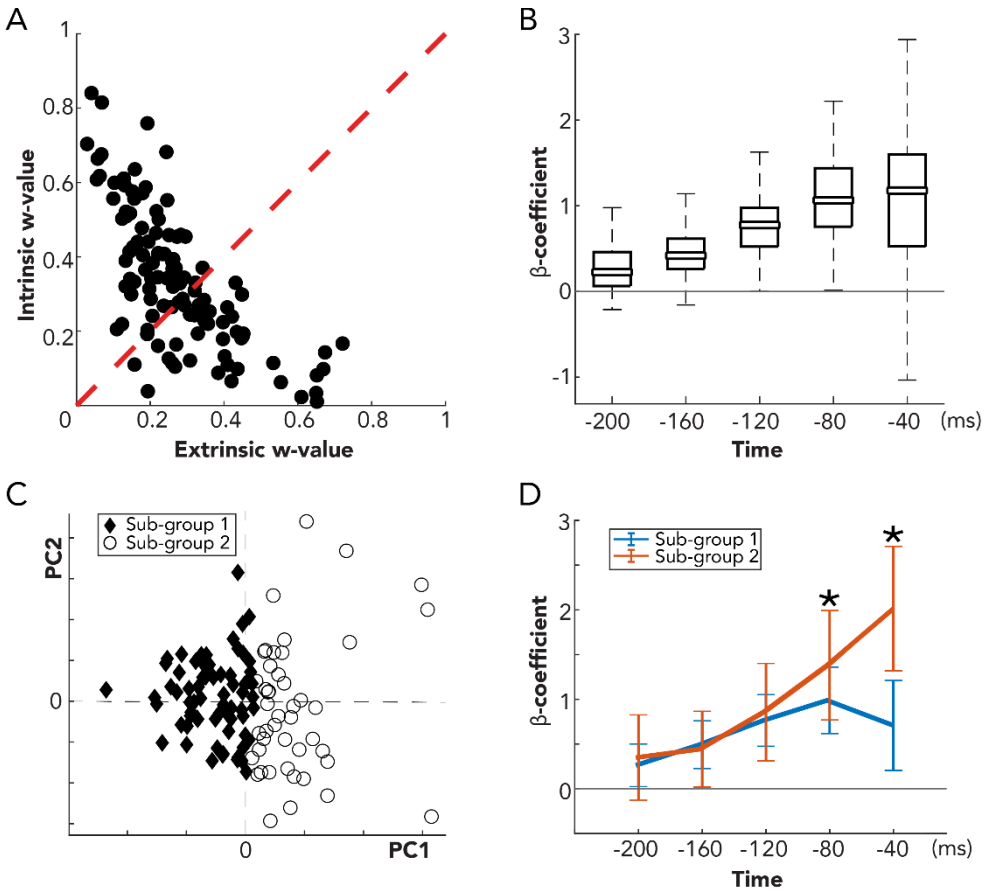

Fig. 19. Influence of spike history on neural activity. A) Extrinsic w-value vs intrinsic w-value (data from M1 and M2 merged). Each dot represents a cell. For dots above the diagonal, spiking activity is predicted better by the intrinsic part of the model rather than the extrinsic one (i.e.,the spike history fits better neural data than extrinsic regressors). X-axis: w-value for the extrinsic part of the model. Y-axis: w-value for the intrinsic part. B) Box plot of spike history beta coefficients in the full model across population. The model includes previous cell neural activity with 5 different time lags (-200, -160, -120, -80, -40 ms) and it estimates a beta coefficient for each lag. C) Representation of the neural population (a symbol for each cell) using the first 2 PCs of the PCA performed on the 5 spike history beta coefficients. Cells are divided in 2 sub-groups running a K-means clustering algorithm on the 5 spike history beta coefficients. D) Mean of the 5 spike history beta coefficients grouping the cells in the 2 sub-groups. Error bars represent the standard deviation and asterisks indicate significant different distributions of beta coefficients between the sub-groups (t-test, p<0.05).

5 DISCUSSION

In this study, we defined how different factors that modulated V6A cells are encoded at single cell level by disentangling them with Poisson GLM. Our model inferred the dependence of activity pattern of each cell from several factors presented together. We obtained a "functional fingerprint" of each cell, that is the ensemble of factors (and their weights) modulating single cell's discharge (see the two example neurons in fig. 15). Present analyses revealed the virtual absence of units modulated by only one parameter. On average, units were selective for 4 different regressor blocks, supporting the view of a mixed selectivity encoding cell discharge in V6A. Next, we moved to the population level to study how neurons encoded spatial parameters along the trial. We found that spatial correlations were higher for neighboring positions and during hold epoch, while temporal correlations were higher and stable from movement preparation to target holding epoch. All these results taken together are coherent with the proposed role of V6A in sensory-motor transformations underlying eye–hand coordination in reaching and grasping.

5.1 Mixed selectivity in V6A

The PPC is implicated in reach-to-grasp movements that are tightly coordinated in space and time. This functionality requires to integrate different inputs (either resulting from internal computation or from sensory information system). An open question is how all these parameters (visual, spatial and somatic) are mixed together to guide coherent behavior. A recent work (Bosco et al., 2019) tried to uncouple contributions of visual information, target position, wrist orientation and grip type in V6A during reach-to-grasp tasks using a demixed PCA technique (Kobak et al., 2016). The authors did separate the contributions of different parameters, but they did not explore how information was mixed at single cell level, a critical step in understanding the sensorimotor transformation, that is addressed by the present thesis.

Theoretically, the encoding process of many inputs could occur following two hypotheses: the area hosts separate, homogeneous groups of cells, each carrying information mainly about one particular feature (or fixed combinations of them) but covering as a whole the encoding of many different features. Alternatively, each cell of the area mixes information relative to many different features in what is called 'mixed selectivity' (Fusi et al., 2016). As demonstrated in this work, V6A contains only very few cells strongly modulated by a specific parameter, while most of them are mildly modulated by many factors. Indeed, the shape of w-values distributions for single blocks of regressors (see fig. 16B) across the population shows a few high values and a gradual decrease towards 0. In particular, for every block of regressors considered, we found an elbow that splits the curve in two parts (highest values vs gradual descent). The shape of this distribution is very similar to that observed by Malik and colleagues (2015). The authors developed a measure that quantifies the tuning

of a neural signal to relevant behavioral variables and found that the distribution of this measure in the motor cortex neural population could be well approximated with the generalized Pareto distribution (Malik et al., 2015). This means that, regardless of how the strength of tuning is calculated (w-value here or Modulation Depth in Malik 2015) and which cortical area is considered, only few cells result strongly modulated for one parameter, the majority of them shows a very low and continuously decreasing modulation.

Previous results on V6A are in accordance with the mixed encoding we found here. In Filippini et al. (2020), for example, authors show that it is possible to decode from the same neural population both the target position and the task phase. As already discussed (see Introduction section), the possibility to decode multiple information from the same ensemble is a characteristic of the mixed selectivity encoding.

Similar results ('mixed selectivity' in parietal areas) were found by Raposo and colleagues in rat PPC (2014), where authors directly tested the hypothesis of the existence of cell types (or categories) within their population. They demonstrated the random distribution of features in what they defined a 'category-free' population, highlighting the possibility for a single network to respond the evolving demands of decision-making.

The hypothesis of a full mixed selectivity seems to be more appropriate to describe V6A. Notably, Zhang and colleagues (2017, 2020) found that another PPC area, AIP, is characterized by what they called 'partial mixed selectivity': among the tested movement parameters, body parts (shoulder or hand) are encoded in two functionally segregated sub-populations within which the other parameters are mixed. In our case, none of the parameters considered in the present work led to a similar segregation, but they were randomly distributed across the population. Future studies should address this issue to investigate whether a similar encoding of effectors is present in area V6A (as in AIP) or whether this area is invariant to body part. While area AIP and the dorsolateral visual stream are more responsible for a finer control of hand configuration during grasping, V6A and the dorsomedial visual stream is active for fast visuospatial computations (Galletti and Fattori, 2018), so we do not expect such a clear-cut segregation between body parts.

The existence of a mixed selectivity encoding in area V6A was predictable considering the multitude of its functional properties (see Introduction) and it had been clearly hypothesized in the past (Battaglia-Mayer et al., 2000). In that study, the authors trained the monkey to perform a variety of different tasks including reaching with/without gaze fixation, saccades and visual stimulations. The idea of a mixed and dynamic neural encoding already emerged there, although it was only qualitatively reported. Indeed, they observed that "the activity of very few cells in this area [V6A] was related in an exclusive fashion to individual retinal, eye, or hand information. On the contrary, the activity of most cells was influenced by all these signals or by different association of them". About 90% (52/57) of V6A neurons showed a high degree of congruence in the preferred directions during the various tasks (saccades, reaching movements…). This phenomenon was defined as 'global tuning field' (Battaglia-Mayer et al., 2000) and it could represent an organizing principle of the neural responses in the context of the otherwise mixed selectivity. Unfortunately, in our study it was not

possible to directly address this issue given the different experimental design. However, the sustained correlations we found from the beginning of the fixation up to the hold phase (fig. 18), suggesting a stable spatial tuning of the population, seem to support this idea, at least during a single foveated reaching task.

From a functional point of view, in higher order areas, we can hypothesize that the selective units receive specialized inputs from other areas and then they spread (working like a distribution hub) the information to neighboring cells. As an alternative, the selective neurons could act as the decoding units that linearly readout the information encoded in the upstream structures to feed the downstream network. The neurons with mixed selectivity, then, compute the information in a mixed way with a complexity that increases with the distance from the source of the inputs. This hypothesis is in accordance with computational models both in parietal and other higher order cortices (Barak et al., 2013; Rigotti et al., 2010; Pouget and Snyder, 2000; Zipser and Andersen, 1988). Theoretically, this process could be repeated several times within the cortex and it could the basis for the information flow from one area to another. Within this framework, whereas it is still possible to find in higher order areas neurons clearly selective for a single, easily identifiable feature, the majority of the population is constituted by neurons that encode many features simultaneously. In this view, past works applying simpler data analysis techniques to study the activity of these areas split the neural populations, that would have been naturally continuous from a functional point of view, in rigid categories (for example, motor vs non-motor neurons, visual vs non-visual neurons, direction selective or non-direction selective neurons and so on) imposing arbitrary thresholds (typically, a $p<0.05$ for most of statistical tests). On one side, this attitude produced much more interpretable experimental results, laying the foundations of all the actual knowledge in neuroscience. However, on the other side, this 'over-simplification' led to neglect the complexity of some neural representations in the name of the interpretability, a complexity that could be the real nature of the neural representations in higher order areas. Thus, recent analytical tools try to account for the majority of complex, mixed modulations rather than focusing only on the selective cells that are highly informative for some aspects but only the tip of the iceberg for others. In this regard, for example, note that the neuron showed in fig. 15A could be defined 'selective' for arm movements, but it represented only a small fraction of V6A cells, laying at one extreme of the distribution of fig. 16D, whereas the majority of units showed more complex discharges.

5.2 The importance of eye and arm movement signals are reflected in the mixed selectivity

Eye-related signals, in particular gaze position signals in 3D space, strongly modulate the activity of V6A neurons (Breveglieri et al., 2014, 2012; Hadjidimitrakis et al., 2011; Galletti et al., 1995) while saccadic eye movements have a weaker influence (Kutz et al. 2003; Battaglia-Mayer et al., 2000). Indeed, in the 'functional fingerprints', EYE-POSITION had high w-values, while EYE SPEED/DIR showed extremely low values. We found transient post-saccadic modulations just after the beginning of fixation (POST SACC block of regressors) and

tonic activity all along fixation (DELAY block of regressors, see below for a further discussion). Relevance of eye position in V6A during reaching has a functional purpose given the pivotal role of V6A in visuomotor transformation. Retinotopic mapping together with eye position can support the reference frame transformation from eye to body-centered frame, required to unfold reach movement (McGuire and Sabes, 2011). Another example of activity strictly dependent from eye position signals is the one showed by V6A neurons with visual receptive field that remains stable in space regardless of eye movements ('real-position' cells; Galletti et al., 1995). It is noteworthy that POST SACC and DELAY could contain information related with maintaining the fixation, but also modulations due to planning activity or spatial attention. Unluckily, our task did not allow us to disentangle the contributions of these processes on neural activity. Beside the high influence of eye signals, we found that also the early phase of arm movement, movement execution and arm holding strongly modulate the activity of V6A cells (high w-values of PREMOV, MOV and HOLD blocks of regressors in fig. 16A). This is coherent with the visuomotor nature of area V6A and its involvement in coordination of reaching movements.

5.3 A dynamic representation of visuospatial information

To investigate how the neural population is spatially tuned along the trial, we performed a correlation analysis on the beta coefficients (Zhang et al., 2017). First, we computed all the correlations between *different targets* within a *fixed epoch*. For all the epochs considered, we found that target spatial positions close to each other are linked by higher correlations than distant positions because, as expected, differences in population activity increased when the distance increased. This trend is consistent with a gain field mechanism which typically plays an important role in multisensory integration, sensorimotor transformations, action planning and visual stability (Morris et al., 2019, 2013; Salinas and Sejnowski, 2001). From a temporal point of view, overall correlations fluctuate along the trial. PREMOV and MOV (fig. 18C) are characterized by low correlation values because cells are more spatially selective during arm movement or just before it, than in other periods of the task. The strongest correlations characterize the HOLD epoch, so the activity is less differentiated between different targets. This can be caused by the similar hand shape and wrist orientation used in the reaching task that can elicit similar responses in the cells sensitive to these parameters (Breveglieri et al., 2018, 2016). Furthermore, since V6A encodes target position, target information is no longer required in hold phase (because the target has already been reached), so it is plausible that some cells tuned for the goal of action are no longer selective during this epoch.

Intermediate correlations are present during DELAY period. This can be explained by two opposite trends: somatosensory inputs of the static position of the arm during HB pressing are the same across all trials and positions eliciting similar somato-sensory discharges in many neurons, while activity is differentiated by spatial attention, motor planning and gaze fixation towards different targets.

Then, we computed the correlations between the *same target* across *subsequent epochs* (fig. 18B and 18D). In the first part of the trial the activity of the population changed rapidly (low or negative correlations) to reach a pattern of activation sustained from the early phases of the movement up to the end of the hold epoch (higher correlations). The results therefore support a switch from a visual code to a more motor-related one or alternatively the superimposition of motor-related and proprioceptive information with previous underlying visual-related inputs. Similar results were recently found in V6A using a decoding analysis (Filippini et al., 2018, 2017). In this case, the authors reported an evolution of visuo- to-motor coding during the execution of reaching and grasping. Moreover, the stability of the correlations found in most epochs is reminiscent of the stability of a mixed body/hand reference frame found in V6A (Hadjidimitrakis et al., 2020). Dynamic processing in PPC is controversial with some works reporting stationary or not-stationary encoding of information (Astrand et al., 2015, Crowe et al. 2010, Meyers et al., 2008). Astrand and colleagues (2015), for example, found that position is encoded statically (i.e., with a persistent pattern of activation) in lateral intraparietal area (LIP), but attention and the cue are encoded dynamically. On the contrary, Crowe and collaborators (2010) reported that the 'side', although being a 'static' information *per sè* in their building task, activated an orderly sequence of activation patterns, thus resulted dynamically encoded in area 7a.
Regarding V6A, the stability of the neural spatial code is highlighted by the results of the correlation analysis here reported. This aspect is confirmed the neural trajectories presented in our recent work (Diomedi et al., 2021): it is possible to identify a dimension (roughly coinciding with the 3° component of the reduced neural space), unique for the entire progression of the task, that allows to separate the different target positions.
Functionally, a certain grade of stability in the spatial encoded information, useful in state estimation and error correction, is coherent with the implication of V6A in the process of comparing the desired position of moving limb with the actual movement (Mendendorp and Heed, 2019; Fattori et al., 2017).

5.4 Different computations may underlie different processing of past activity

We showed that the spike history (intrinsic block of regressors) explains neural activity better than the extrinsic part of the model (see intrinsic w-values vs extrinsic w-values in fig. 19A). This can be due to the result of the complex internal processes of the area (Takahashi et al., 2017). Notice that the spike history is only indirectly related to the ongoing task and behavior and, thus, it could account for neural modulations caused by uncontrolled parameters (and so not directly included in the model as regressors). These modulations may be either internal (for instance, general state of attention or local circuitry) and external (e.g. kinematics and kinetics or fatigue) to the brain. Among these hypothetical contributions, attentional modulations are known to affect V6A activity in human and monkey brains (Caspari et al 2018, 2015; Ciavarro et al., 2013; Galletti et al., 2010) and thus they likely play a central role, but our task did not allow to disentangle them from other processes.

We then wondered whether contribution of past activity was different moving away from actual time. It turned out that the most recent spike history (the last 80 ms approximately) had a high influence on the firing rate of the neurons, whereas previous activity was much less predictive of the actual discharge, or not predictive at all. This finding is coherent, for example, with the integration timescale proposed for single neurons in the nearby parietal area LIP (aprox. 70 ms; Spitmaan et al., 2020) and in visual cortex (aprox. 80 ms; Resulaj et al., 2018). We observed two main trends within our V6A cell population: some units were more affected by the influence of past activity, whereas others were not. The transition between these two sub-groups was continuous and smooth, thus it was not possible to clearly identify a cutoff between two clusters. Accordingly, even if the two types of encoding were 'mixed' in the neural population, to stress these different trends we divided the population in two sub-groups that essentially differed for the importance of the activity in the last 80ms: a first sub-group with an increasing positive influence approaching current time and a second sub-group where the past activity influence had quite constant and generally lower values. A possible explanation for these different patterns could be traced back to functional differences. Neurons with a ramp-like activity pattern are common in PPC and could be mainly represented in the first sub-group, supporting progressive sensorimotor transformations and/or intra-area computing. In the second group, the neurons were less modulated by past activity and therefore they could be part of an online control network, working as comparator between expected and actual movement, a task that requires updating information with a high 'refresh rate' and thus shorter operating timescales (Medendorp and Heed, 2019; Fattori et al., 2017). Firing rates in this case could reflect faster transient activity such as afferent feedback signals from the premotor cortex (found in V6A, see Passarelli et al., 2011; Gamberini et al., 2009). The possibility that PPC works as a state estimator with an internal forward model constantly updated by different sensory inputs (Mendendorp and Heed, 2019) makes the existence of different subpopulations with different functions plausible. However, further studies are needed to elucidate their functions.

Interestingly, in recurrent neural networks it has been shown that the recurrency of the signals apparently introduces more chaos in the population activity (Luccioli et al., 2012; Monteforte and Wolf, 2010; Latham et al., 2000), but it serves to distribute the information across the network so that stimuli can be classified based on only a small sub-population of readout neurons (Lajoie et al., 2016). As already discussed (see Introduction), the information distributed across the entire population and the capacity to simply readout from subset of neurons (and vice versa, from a neural ensemble to readout several information relevant to perform different tasks) are important correlates of mixed selectivity. These aspects are linked at single-cell level introducing the spiking history that represents a form of recurrency. Thus, the units we found to encode more strongly their previous spiking history could play a central role in distributing the information across the network and building a mixed selectivity encoding.

5.5 Brain Machine Interface implications

A brain machine interface (BMI) is a device that connects the brain with computers and other electronics and can be used to assist subjects with impaired capabilities due to neurological deficits. Nowadays, two types of BMIs are available: 'write-in' systems that, typically through electrical stimulation, send inputs to the brain (for example, cochlear implants) and 'read-out' systems that can decode brain activity (often in the form of action potentials) to control external devices such as a computer, a robotic limb or a wheelchair, assisting paralyzed patients.

In the case of parietal areas, neural activity seems very suited to be used in neuroprosthetics for motor control. Although up to now most of the motor BMI have used signals from motor cortex (Hatsopoulos and Donoghue, 2009; Lebedev and Nicolelis, 2006; Schwartz, 2004), known to encode limb movement trajectories and which is close to the motor output, parietal regions offer few advantages (Andersen et al., 2014). First, they seem to contain the 'intent' to make movements at a higher, cognitive level and the goal of the action, that would be interesting for fast computations. Second, since this region contains bilateral representations of limbs movements, conversely to somatosensory areas or motor cortex, a single implant could extract information about bimanual actions. Indeed, although the neurons modulated by the contralateral arm are prevalent also in these areas, the neural representation of the ipsilateral limb is still consistent and it can be readily extracted by a BMI (Zhang et al., 2020). In addition, PPC has been reported to encode for sequence of goal-directed movements (Baldauf et al., 2008) that could be eventually decoded at once.

According to this idea, in the last years, efforts have been done to decode the parietal activity, a necessary step to drive a neuroprothesis. From the population activity of area V6A, the information about the target position and the task phases have already been efficiently extracted (Filippini et al., 2020, 2018). The neural signals coming from other parietal areas, such as area 5 (PE) and MIP, had been previously decoded to allow a monkey to move a cursor without any apparent motor output (Mulliken et al., 2008; Musallam et al., 2004). A few PPC areas remain unexplored (such as PEc, PEip and PGm) and an interesting outcome of the analysis here presented could be the selection of the parietal areas more suitable to extract information about specific parameters.

Alternatively, the functional fingerprints could be used to feed a neurodecoder with only the units more selective to the features relevant for the specific task requirements with a great computational advantage. The cell selection process based on the 'functional fingerprint' would require a pre-analysis of the information available from an electrode array to fit the GLMs and then retain the best coding neurons. Indeed, selective neuron dropping to remove the noisier units has been proved to maintain a performance similar to the one obtained from the entire data set (about the 90% of the maximal performance retaining only 10 neurons over almost 200), but with a great decrease in the computational load (Sanchez et al., 2004).

5.6 Limitations and future directions

The task used in the present work (fix-to-reach) allowed us to study the effect on cell discharge of brief saccadic eye movement to foveate the target, eye position, arm-movement preparation, direction and extent of arm movement, and spatial position of the extended arm in the peripersonal space. Our foveal task (see Methods) does not allow to study separately the effects of spatial attention and motor planning, while both factors are known to strongly influence the activity of many V6A cells (Fattori et al. 2017, Breveglieri et al., 2014, Galletti et al. 2010). Due to the high variable timing of these processes between one cell and another, traces of their modulations were taken into account by few blocks of regressors (POST SACC, DELAY and PREP; see above).

Moreover, we did not record reaching kinematics during the task, therefore our model does not incorporate movement regressors that can describe arm position and joints rotation. Since somatosensory cells are present in V6A (Gamberini et al., 2018; Breveglieri et al., 2002), future works could enhance our actual GLM with arm movement descriptors to test how finely this area is involved in the control of arm movements.

This thesis focused on the neural rate coding that consider the firing rate as the channel via which the neurons communicate and convey information. Another possible coding scheme is the temporal code, based on the synchrony (or latency) of the spikes rather their occurrence frequency (Cariani, 1997). In this work, we did not consider temporal coding because it is extremely less studied and mostly because the nature of our non-simultaneous electrophysiological recordings did not allow to consider temporal synchronies on the scale of a few milliseconds.

To summarize, the study analyzed in detail many different parameters known to modulate area V6A during a reaching task. Several GLMs for each cell were fitted to explain neural modulations. From these models, it has been possible to compute the weight that each feature has on the cells to extract information about the type of neural encoding. Our results suggest that V6A encodes reaching parameters in a “mixed” fashion, with single cells forming a continuous functional spectrum and with no evidence of any segregation.

6 REFERENCES

Andersen, R. A., Kellis, S., Klaes, C., & Aflalo, T. (2014). Toward more versatile and intuitive cortical brain-machine interfaces. Current biology : CB, 24(18), R885–R897.Andersen, R. A., & Cui, H. (2009). Intention, action planning, and decision making in parietal-frontal circuits. Neuron, 63(5), 568–583.

Andersen, R. A., & Cui, H. (2009). Intention, action planning, and decision making in parietal-frontal circuits. Neuron, 63(5), 568–583.

Andersen, R. A., Snyder, L. H., Bradley, D. C., & Xing, J. (1997). Multimodal representation of space in the posterior parietal cortex and its use in planning movements. Annual review of neuroscience, 20, 303–330.

Astrand, E., Ibos, G., Duhamel, J. R., Ben Hamed, S. (2015). Differential dynamics of spatial attention, position, and color coding within the parietofrontal network. J. Neurosci. 35(7), 3174–3189.

Bakola, S., Passarelli, L., Huynh, T., Impieri, D., Worthy, K. H., Fattori, P., Galletti, C., Burman, K. J., & Rosa, M. (2017). Cortical Afferents and Myeloarchitecture Distinguish the Medial Intraparietal Area (MIP) from Neighboring Subdivisions of the Macaque Cortex. eNeuro, 4(6), ENEURO.0344-17.2017.

Bakola, S., Gamberini, M., Passarelli, L., Fattori, P., & Galletti, C. (2010). Cortical connections of parietal field PEc in the macaque: linking vision and somatic sensation for the control of limb action. Cerebral cortex (New York, N.Y. : 1991), 20(11), 2592–2604.

Baldauf, D., Cui, H., and Andersen, R.A. (2008). The posterior parietal cortex encodes in parallel both goals for double-reach sequences. J. Neurosci. 28, 10081–10089.

Barak, O., Rigotti, M., Fusi, S., (2013). The Sparseness of Mixed Selectivity Neurons Controls the Generalization–Discrimination Trade-Off. J. Neurosci. 33, 3844–3856.

Batista, A. P., Buneo, C. A., Snyder, L. H., & Andersen, R. A. (1999). Reach plans in eye-centered coordinates. Science (New York, N.Y.), 285(5425), 257–260.

Battaglia-Mayer, A., Ferraina, S., Genovesio, A., Marconi, B., Squatrito, S., Molinari, M., Lacquaniti, F., & Caminiti, R. (2001). Eye-hand coordination during reaching. II. An analysis of the relationships between visuomanual signals in parietal cortex and parieto-frontal association projections. Cerebral cortex (New York, N.Y. : 1991), 11(6), 528–544.

Battaglia-Mayer, A., Ferraina, S., Mitsuda, T., Marconi, B., Genovesio, A., Onorati, P., Lacquaniti, F., & Caminiti, R. (2000). Early coding of reaching in the parietooccipital cortex. Journal of neurophysiology, 83(4), 2374–2391.

Baumann, M. A., Fluet, M. C., & Scherberger, H. (2009). Context-specific grasp movement representation in the macaque anterior intraparietal area. The Journal of neuroscience : the official journal of the Society for Neuroscience, 29(20), 6436–6448.

Bosco, A., Breveglieri, R., Filippini, M., Galletti, C., Fattori, P., (2019). Reduced neural representation of arm / hand actions in the medial posterior parietal cortex. Sci. Rep. 1–14.

Bosco, A., Breveglieri, R., Chinellato, E., Galletti, C., Fattori, P., (2010). Reaching activity in the medial posterior parietal cortex of monkeys is modulated by visual feedback. J Neurosci 30, 14773–14785.

Braitenberg, V. & Schüz, A. (1998). Cortex: Statistics and Geometry of Neuronal Connectivity 2nd edn (Springer).

Breveglieri, R., De Vitis, M., Bosco, A., Galletti, C., Fattori, P., (2018). Interplay Between Grip and Vision in the Monkey Medial Parietal Lobe. Cereb. Cortex 1–15.

Breveglieri, R., Bosco, A., Galletti, C., Passarelli, L., Fattori, P., (2016). Neural activity in the medial parietal area V6A while grasping with or without visual feedback. Sci. Rep. 6, 28893.

Breveglieri, R., Galletti, C., Bò, G.D., Hadjidimitrakis, K., Fattori, P., (2014). Multiple Aspects of Neural Activity during Reaching Preparation in the Medial Posterior Parietal Area V6A. J. Cogn. Neurosci. 878–895.

Breveglieri, R., Hadjidimitrakis, K., Bosco, A., Sabatini, S., Galletti, C., Fattori, P., (2012). Eye Position Encoding in Three-Dimensional Space: Integration of Version and Vergence Signals in the Medial Posterior Parietal Cortex. J. Neurosci. 32, 159–169.

Breveglieri, R., Galletti, C., Gamberini, M., Passarelli, L., & Fattori, P. (2006). Somatosensory cells in area PEc of macaque posterior parietal cortex. The Journal of neuroscience : the official journal of the Society for Neuroscience, 26(14), 3679–3684.

Breveglieri, R., Kutz, D. F., Fattori, P., Gamberini, M., Galletti, C. (2002). Somatosensory cells in the parieto-occipital area V6A of the macaque. Neuroreport, 13(16), 2113–2116.

Brown, L. E., Halpert, B. A., & Goodale, M. A. (2005). Peripheral vision for perception and action. Experimental brain research, 165(1), 97–106.

Buonomano, D. V., & Maass, W. (2009). State-dependent computations: spatiotemporal processing in cortical networks. Nature reviews. Neuroscience, 10(2), 113–125.

Cameron, A.C., & Windmeijer, F.A.G., (1997). An R-squared measure of goodness of fit for some common nonlinear regression models. J. Econom. 77, 329–342.

Caminiti, R., Innocenti, G. M., & Battaglia-Mayer, A. (2015). Organization and evolution of parieto-frontal processing streams in macaque monkeys and humans. Neuroscience and biobehavioral reviews, 56, 73–96.

Caminiti, R., Genovesio, A., Marconi, B., Mayer, A. B., Onorati, P., Ferraina, S., Mitsuda, T., Giannetti, S., Squatrito, S., Maioli, M. G., & Molinari, M. (1999). Early coding of reaching: frontal and parietal association connections of parieto-occipital cortex. The European journal of neuroscience, 11(9), 3339–3345.

Cariani, P.A. (1997). Temporal coding of sensory information. In: Bower, J.M. (eds) Computational Neuroscience. Springer, Boston, MA.

Caspari, N., Arsenault, J.T., Vandenberghe, R., & Vanduffel, W., (2018). Functional Similarity of Medial Superior Parietal Areas for Shift-Selective Attention Signals in Humans and Monkeys. Cereb. Cortex 2085–2099.

Caspari, N., Janssens, T., Mantini, D., Vandenberghe, R., & Vanduffel, W., (2015). Covert Shifts of Spatial Attention in the Macaque Monkey. J. Neurosci. 35, 7695–7714.

Cavada C. (2001). The visual parietal areas in the macaque monkey: current structural knowledge and ignorance. NeuroImage, 14(1 Pt 2), S21–S26.

Colby, C.L., Gattass, R., Olson, C.R. & Gross, C.G. (1988). Topographical organization of cortical afferents to extrastriate visual area PO in the macaque: a dual tracer study. J. Comp. Neurol., 269, 392–413.

Churchland, M. M., & Shenoy, K. V. (2007). Temporal complexity and heterogeneity of single-neuron activity in premotor and motor cortex. Journal of neurophysiology, 97(6), 4235–4257.

Ciavarro, M., Ambrosini, E., Tosoni, A., Committeri, G., Fattori, P., Galletti, G., (2013). rTMS of Medial Parieto-occipital Cortex Interferes with Attentional Reorienting during Attention and Reaching Tasks. J. Cogn. Neurosci. 25:9,1453–1462.

Covey, E., Gattass, R. & Gross, C.G. (1982). A new visual area in the parietooccipital sulcus of the macaque. Abstract Soc. Neurosci., 8, 681.

Crowe, D.A., Averbeck, B.B., Chafee, M.V. (2010). Rapid sequences of population activity patterns dynamically encode task-critical spatial information in parietal cortex. J. Neurosci., 30(35), 11640–11653.

Danckert, J., & Goodale, M. A. (2001). Superior performance for visually guided pointing in the lower visual field. Experimental brain research, 137(3-4), 303–308.

Dayan, P., Abbott, L.F., (2001). Theoretical Neuroscience - Computational and Mathematical Modeling of Neural Systems (The MIT Press).

De Vitis, M., Breveglieri, R., Hadjidimitrakis, K., Vanduffel, W., Galletti, C., & Fattori, P. (2019). The neglected medial part of macaque area PE: segregated processing of reach depth and direction. Brain structure & function, 224(7), 2537–2557.

Diomedi, S., Vaccari, F. E., Galletti, C., Hadjidimitrakis, K., & Fattori, P. (2021). Motor-like neural dynamics in two parietal areas during arm reaching. Progress in neurobiology, 205, 102116.

Diomedi, S., Vaccari, F. E., Filippini, M., Fattori, P., & Galletti, C. (2020). Mixed Selectivity in Macaque Medial Parietal Cortex during Eye-Hand Reaching. iScience, 23(10), 101616.

Duhamel, J. R., Colby, C. L., & Goldberg, M. E. (1998). Ventral intraparietal area of the macaque: congruent visual and somatic response properties. Journal of neurophysiology, 79(1), 126–136.

Fattori, P., Breveglieri, R., Bosco, A., Gamberini, M., Galletti, C., (2017). Vision for prehension in the medial parietal cortex. Cereb. Cortex 27, 1149–1163.

Fattori, P., Breveglieri, R., Marzocchi, N., Maniadakis, M., & Galletti, C., (2007). Brain Area V6A: A Cognitive Model for an Embodied Artificial Intelligence. In: Lungarella M., Iida F., Bongard J., Pfeifer R. (eds) 50 Years of Artificial Intelligence. Lecture Notes in Computer Science, vol 4850. Springer, Berlin, Heidelberg.

Fattori, P., Kutz, D.F., Breveglieri, R., Marzocchi, N., Galletti, C., (2005). Spatial tuning of reaching activity in the medial parieto-occipital cortex (area V6A) of macaque monkey. Eur. J. Neurosci. 22, 956–72.

Filimon F. (2010). Human cortical control of hand movements: parietofrontal networks for reaching, grasping, and pointing. The Neuroscientist : a review journal bringing neurobiology, neurology and psychiatry, 16(4), 388–407.

Filippini, M., Morris, A. P., Breveglieri, R., Hadjidimitrakis, K., & Fattori, P. (2020). Decoding of standard and non-standard visuomotor associations from parietal cortex. Journal of neural engineering, 17(4), 046027.

Filippini, M., Breveglieri, R., Hadjidimitrakis, K., Bosco, A., Fattori, P. (2018). Prediction of Reach Goals in Depth and Direction from the Parietal Cortex. Cell reports, 23(3), 725–732.

Filippini, M., Breveglieri, R., Akhras, M.A., Bosco, A., Chinellato, E., Fattori, P. (2017). Decoding Information for Grasping from the Macaque Dorsomedial Visual Stream. J Neurosci. 37(16), 4311–4322.

Finkelstein, A., Ulanovsky, N., Tsodyks, M., & Aljadeff, J. (2018). Optimal dynamic coding by mixed-dimensionality neurons in the head-direction system of bats. Nature communications, 9(1), 3590.

Freedman, D. J., & Assad, J. A. (2009). Distinct encoding of spatial and nonspatial visual information in parietal cortex. The Journal of neuroscience: the official journal of the Society for Neuroscience, 29(17), 5671–5680.

Fusi, S., Miller, E.K., Rigotti, M., (2016). Why neurons mix: high dimensionality for higher cognition. Curr. Opin. Neurobiol. 37, 66–74.

Galletti, C., Fattori, P., (2018). The dorsal visual stream revisited: Stable circuits or dynamic pathways? Cortex 98, 203–217.

Galletti, C., Breveglieri, R., Lappe, M., Bosco, A., Ciavarro, M., Fattori, P., (2010). Covert shift of attention modulates the ongoing neural activity in a reaching area of the macaque dorsomedial visual stream. PLoS One 5, e15078.

Galletti, C., Gamberini, M., Kutz, D. F., Baldinotti, I., & Fattori, P. (2005). The relationship between V6 and PO in macaque extrastriate cortex. The European journal of neuroscience, 21(4), 959–970.

Galletti, C., Kutz, D.F., Gamberini, M., Breveglieri, R., Fattori, P., (2003). Role of the medial parieto-occipital cortex in the control of reaching and grasping movements. Exp. Brain Res. 153, 158–170.

Galletti, C., Fattori, P., Kutz, D.F., Gamberini, M., (1999). Brain location and visual topography of cortical area V6A in the macaque monkey. Eur. J. Neurosci. Vol. 11, 575-582.

Galletti C, Fattori P, Kutz DF, Battaglini PP (1997) Arm movement-related neurons in the visual area V6A of the macaque superior parietal lobule. Eur J Neurosci 9:410–413.

Galletti, C., Fattori, P., Battaglini, P. P., Shipp, S., & Zeki, S. (1996). Functional demarcation of a border between areas V6 and V6A in the superior parietal gyrus of the macaque monkey. The European journal of neuroscience, 8(1), 30–52.

Galletti, C., Battaglini, P.P., Fattori, P., (1995). Eye Position Influence on the Parieto-occipital Area PO (V6) of the Macaque Monkey. European Journal of Neuroscience 7(12).

Gamberini, M., Passarelli, L., Fattori, P., Galletti, C., (2020). Structural connectivity and functional properties of the macaque superior parietal lobule. Brain Struct Funct. 225(4):1349-1367.

Gamberini, M., Dal Bò, G., Breveglieri, R., Briganti, S., Passarelli, L., Fattori, P., Galletti, C., (2018). Sensory properties of the caudal aspect of the macaque's superior parietal lobule. Brain Struct. Funct. 223, 1863–1879.

Gamberini, M., Galletti, C., Bosco, A., Breveglieri, R., Fattori, P., (2011). Is the medial posterior parietal area V6A a single functional area? J. Neurosci. 31, 5145–57.

Gamberini, M., Passarelli, L., Fattori, P., Zucchelli, M., Bakola, S., Luppino, G., Galletti, C. (2009). Cortical connections of the visuomotor parietooccipital area V6Ad of the macaque monkey. The Journal of comparative neurology, 513(6), 622–642.

Gattass, R., Sousa, A.P.B. & Covey, E. (1986). Cortical visual areas of the macaque: possible substrates for pattern recognition mechanisms. Exp. Brain Res. Suppl., 11, 1–20.

Ghahremani, M., Hutchison, R. M., Menon, R. S., & Everling, S. (2017). Frontoparietal Functional Connectivity in the Common Marmoset. Cerebral cortex (New York, N.Y. : 1991), 27(8), 3890–3905.

Goodman, J.M., Tabot, G.A., Lee, A.S., Suresh, A.K., Rajan, A.T., Hatsopoulos, N.G., Bensmania, S., (2019). Postural Representations of the Hand in the Primate Sensorimotor Cortex Article Postural Representations of the Hand in the Primate Sensorimotor Cortex. Neuron 104, 1000-1009.e7.

Gottlieb J. (2007). From thought to action: the parietal cortex as a bridge between perception, action, and cognition. Neuron, 53(1), 9–16.

Graziano, M. S., & Cooke, D. F. (2006). Parieto-frontal interactions, personal space, and defensive behavior. Neuropsychologia, 44(13), 2621–2635.

Hadjidimitrakis, K., Ghodrati, M., Breveglieri, R., Rosa, M.G.P., Fattori, P., (2020). Neural coding of action in three dimensions: Task- and time-invariant reference frames for visuospatial and motor-related activity in parietal area V6A. J Comp Neurol.10.1002/cne.24889.

Hadjidimitrakis, K., Bakola, S., Wong, Y.T., Hagan, M.A. (2019). Mixed Spatial and Movement Representations in the Primate Posterior Parietal Cortex. Frontiers in neural circuits, 13, 15.

Hadjidimitrakis, K., Bertozzi, F., Breveglieri, R., Galletti, C., Fattori, P., (2017). Temporal stability of reference frames in monkey area V6A during a reaching task in 3D space. Brain Struct. Funct. 222, 1959–1970.

Hadjidimitrakis, K., Bertozzi, F., Breveglieri, R., Bosco, A., Galletti, C., Fattori, P., (2014). Common neural substrate for processing depth and direction signals for reaching in the monkey medial posterior parietal cortex. Cereb. Cortex 24, 1645–57.

Hadjidimitrakis, K., Breveglieri, R., Placenti, G., Bosco, A., Sabatini, S.P., Fattori, P., (2011). Fix Your Eyes in the Space You Could Reach: Neurons in the Macaque Medial Parietal Cortex Prefer Gaze Positions in Peripersonal Space. PLoS One 6, e23335.

Harvey, C. D., Coen, P., & Tank, D. W. (2012). Choice-specific sequences in parietal cortex during a virtual-navigation decision task. Nature, 484(7392), 62–68.

Hatsopoulos, N.G., and Donoghue, J.P. (2009). The science of neural interface systems. Annu. Rev. Neurosci. 32, 249–266.

Hatsopoulos, N. G., Xu, Q., & Amit, Y. (2007). Encoding of movement fragments in the motor cortex. The Journal of neuroscience : the official journal of the Society for Neuroscience, 27(19), 5105–5114.

Jaeger, H., & Haas, H. (2004). Harnessing nonlinearity: predicting chaotic systems and saving energy in wireless communication. Science (New York, N.Y.), 304(5667), 78–80.

Joelving, F. C., Compte, A., & Constantinidis, C. (2007). Temporal properties of posterior parietal neuron discharges during working memory and passive viewing. Journal of neurophysiology, 97(3), 2254–2266.

Johnston, W. J., Palmer, S. E., & Freedman, D. J. (2020). Nonlinear mixed selectivity supports reliable neural computation. PLoS computational biology, 16(2), e1007544.

Kalaska, J. F., Scott, S. H., Cisek, P., & Sergio, L. E. (1997). Cortical control of reaching movements. Current opinion in neurobiology, 7(6), 849–859.

Kalaska, J. F., Caminiti, R., & Georgopoulos, A. P. (1983). Cortical mechanisms related to the direction of two-dimensional arm movements: relations in parietal area 5 and comparison with motor cortex. Experimental brain research, 51(2), 247–260.

Kobak, D., Brendel, W., Constantinidis, C., Feierstein, C. E., Kepecs, A., Mainen, Z. F., Qi, X. L., Romo, R., Uchida, N., Machens, C. K. (2016). Demixed principal component analysis of neural population data. eLife, 5, e10989.

Kutz, D.F., Marzocchi, N., Fattori, P., Cavalcanti, S., Galletti, C., (2005). Real-Time Supervisor System Based on Trinary Logic to Control Experiments with Behaving Animals and Humans. J. Neurophysiol. 93, 3674–3686.

Kutz, D.F., Fattori, P., Gamberini, M., Breveglieri, R., Galletti, C., (2003). Early- and late-responding cells to saccadic eye movements in the cortical area V6A of macaque monkey. Exp Brain Res 83–95.

Lajoie, G., Lin, K. K., Thivierge, J. P., & Shea-Brown, E. (2016). Encoding in Balanced Networks: Revisiting Spike Patterns and Chaos in Stimulus-Driven Systems. PLoS computational biology, 12(12), e1005258.

Latham, P. E., Richmond, B. J., Nelson, P. G., & Nirenberg, S. (2000). Intrinsic dynamics in neuronal networks. I. Theory. Journal of neurophysiology, 83(2), 808–827.

Lebedev, M.A., & Nicolelis, M.A. (2006). Brain-machine interfaces: past, present and future. Trends Neurosci. 29, 536–546.

Lehmann, S.J., & Scherberger, H., (2013). Reach and gaze representations in macaque parietal and premotor grasp areas. J. Neurosci. 33, 7038–49.

Luccioli, S., Olmi, S., Politi, A., & Torcini, A. (2012). Collective dynamics in sparse networks. Physical review letters, 109(13), 138103.

Luppino, G., Ben Hamed, S., Gamberini, M., Matelli, M., Galletti, C., (2005). Occipital (V6) and parietal (V6A) areas in the anterior wall of the parieto-occipital sulcus of the macaque: A cytoarchitectonic study. Eur. J. Neurosci. 21, 3056–3076.

Maass, W., Natschläger, T., & Markram, H. (2002). Real-time computing without stable states: a new framework for neural computation based on perturbations. Neural computation, 14(11), 2531–2560.

Maimon, G., & Assad, J. A. (2009). Beyond Poisson: increased spike-time regularity across primate parietal cortex. Neuron, 62(3), 426–440.

Malik, W., Hochberg, L., Donoghue, J., Brown, E., (2015). Modulation Depth Estimation and Variable Selection in State- Space Models for Neural Interfaces. IEEE Trans Biomed Eng 62(2), 570–581.

Marconi, B., Genovesio, A., Battaglia-Mayer, A., Ferraina, S., Squatrito, S., Molinari, M., Lacquaniti, F., & Caminiti, R. (2001). Eye-hand coordination during reaching. I. Anatomical relationships between parietal and frontal cortex. Cerebral cortex (New York, N.Y. : 1991), 11(6), 513–527.

Marzocchi, N., Breveglieri, R., Galletti, C., Fattori, P., (2008). Reaching activity in parietal area V6A of macaque: Eye influence on arm activity or retinocentric coding of reaching movements? Eur. J. Neurosci. 27, 775–789.

Matelli, M., Govoni, P., Galletti, C., Kutz, D. F., & Luppino, G. (1998). Superior area 6 afferents from the superior parietal lobule in the macaque monkey. The Journal of comparative neurology, 402(3), 327–352.

McGuire, L.M.M., Sabes, P.N., (2011). Heterogeneous Representations in the Superior Parietal Lobule Are Common across Reaches to Visual and Proprioceptive Targets. J. Neurosci. 31(18) 6661-6673.

Medendorp, W.P., Heed, T., (2019). State estimation in posterior parietal cortex: Distinct poles of environmental and bodily states. Progress in neurobiology, 183, 101691.

Meister, M. L., Hennig, J. A., & Huk, A. C. (2013). Signal multiplexing and single-neuron computations in lateral intraparietal area during decision-making. The Journal of neuroscience: the official journal of the Society for Neuroscience, 33(6), 2254–2267.

Meyers, E. M., Freedman, D. J., Kreiman, G., Miller, E.K., Poggio, T., (2008). Dynamic population coding of category information in inferior temporal and prefrontal cortex. Journal of neurophysiology, 100(3), 1407–1419.

Mittal, A. M., Gupta, D., Singh, A., Lin, A. C., & Gupta, N. (2020). Multiple network properties overcome random connectivity to enable stereotypic sensory responses. Nature communications, 11(1), 1023.

Monteforte, M., & Wolf, F. (2010). Dynamical entropy production in spiking neuron networks in the balanced state. Physical review letters, 105(26), 268104.

Morris, A.P., & Krekelberg, B., (2019). A Stable Visual World in Primate Primary Visual Cortex. Curr Biol. 29(9):1471-1480.e6.

Morris, A.P., & Bremmer, F., Krekelberg, B. (2013). Eye-position signals in the dorsal visual system are accurate and precise on short timescales. J. Neurosci., 33(30), 12395–12406.

Mulliken, G. H., Musallam, S., & Andersen, R. A. (2008). Decoding trajectories from posterior parietal cortex ensembles. The Journal of neuroscience : the official journal of the Society for Neuroscience, 28(48), 12913–12926.

Murata, A., Gallese, V., Luppino, G., Kaseda, M., & Sakata, H. (2000). Selectivity for the shape, size, and orientation of objects for grasping in neurons of monkey parietal area AIP. Journal of neurophysiology, 83(5), 2580–2601.

Musallam, S., Corneil, B. D., Greger, B., Scherberger, H., & Andersen, R. A. (2004). Cognitive control signals for neural prosthetics. Science (New York, N.Y.), 305(5681), 258–262.

Nakamura, K., Chung, H. H., Graziano, M. S., & Gross, C. G. (1999). Dynamic representation of eye position in the parieto-occipital sulcus. Journal of neurophysiology, 81(5), 2374–2385.

Paninski, L., Fellows, M.R., Hatsopoulos, N.G., and Donoghue, J.P., (2004a). Spatiotemporal tuning of motor cortical neurons for hand position and velocity. J. Neurophysiol. 91, 515–532.

Paninski, L., (2004b). Maximum likelihood estimation of cascade point-process neural encoding models. Netw. Comput. Neural Syst. 15, 243–262.

Parthasarathy, A., Herikstad, R., Bong, J.H., Medina, F.S., Libedinsky, C., Yen, S.C., (2017). Mixed selectivity morphs population codes in prefrontal cortex. Nat. Neurosci. 20, 1770–1779.

Pascanu, R., & Jaeger, H. (2011). A neurodynamical model for working memory. Neural networks : the official journal of the International Neural Network Society, 24(2), 199–207.

Passarelli, L., Rosa, M. G., Gamberini, M., Bakola, S., Burman, K. J., Fattori, P., Galletti, C. (2011). Cortical connections of area V6Av in the macaque: a visual-input node to the eye/hand coordination system. J. Neurophysiol. 31(5), 1790–1801.

Pillow, J.W., Shlens, J., Paninski, L., Sher, A., Litke, A.M., Chichilnisky, E.J., Simoncelli, E.P., (2008). Spatio-temporal correlations and visual signalling in a complete neuronal population. Nature.

Pisella, L., Rossetti, Y., & Rode, G. (2017). Optic ataxia in Bálint-Holmes syndrome. Annals of physical and rehabilitation medicine, 60(3), 148–154.

Pitzalis, S., Fattori, P., & Galletti, C. (2015). The human cortical areas V6 and V6A. Visual neuroscience, 32, E007.

Pitzalis, S., Sereno, M. I., Committeri, G., Fattori, P., Galati, G., Tosoni, A., & Galletti, C. (2013). The human homologue of macaque area V6A. NeuroImage, 82, 517–530.

Pitzalis, S., Sereno, M. I., Committeri, G., Fattori, P., Galati, G., Patria, F., & Galletti, C. (2010). Human v6: the medial motion area. Cerebral cortex (New York, N.Y. : 1991), 20(2), 411–424.

Pitzalis, S., Galletti, C., Huang, R. S., Patria, F., Committeri, G., Galati, G., Fattori, P., & Sereno, M. I. (2006). Wide-field retinotopy defines human cortical visual area v6. The Journal of neuroscience : the official journal of the Society for Neuroscience, 26(30), 7962–7973.

Pouget, A., & Snyder, L.H., (2000). Computational approaches to sensorimotor transformations. Nat. Neurosci. 3 Suppl:1192-8.

Premereur, E., Vanduffel, W., & Janssen, P. (2011). Functional heterogeneity of macaque lateral intraparietal neurons. *The Journal of neuroscience : the official journal of the Society for Neuroscience*, *31*(34), 12307–12317.

Raposo, D., Kaufman, M. & Churchland, A. (2014). A category-free neural population supports evolving demands during decision-making. Nat Neurosci 17, 1784–1792.

Rentzeperis, I., Nikolaev, A. R., Kiper, D. C., & van Leeuwen, C. (2014). Distributed processing of color and form in the visual cortex. Frontiers in psychology, 5, 932.

Resulaj, A., Ruediger, S., Olsen, S. R., & Scanziani, M. (2018). First spikes in visual cortex enable perceptual discrimination. eLife, 7, e34044.

Rigotti, M., Barak, O., Warden, M.R., Wang, X., Nathaniel, D., Miller, E.K., Fusi, S., (2013). The importance of mixed selectivity in complex cognitive tasks. Nature 497, 585–590.

Rigotti, M., Rubin, D.B.D., Wang, X., Fusi, S., (2010). Internal representation of task rules by recurrent dynamics: the importance of the diversity of neural responses. Front. Comput. Neurosci. 4, 1–29.

Rishel, C. A., Huang, G., & Freedman, D. J. (2013). Independent category and spatial encoding in parietal cortex. Neuron, 77(5), 969–979.

Rizzolatti, G., & Luppino, G. (2001). The cortical motor system. Neuron, 31(6), 889–901.

Romero, M. C., Pani, P., & Janssen, P. (2014). Coding of shape features in the macaque anterior intraparietal area. *The Journal of neuroscience : the official journal of the Society for Neuroscience*, *34*(11), 4006–4021.

Romero, M. C., Van Dromme, I., & Janssen, P. (2012). Responses to two-dimensional shapes in the macaque anterior intraparietal area. *The European journal of neuroscience*, *36*(3), 2324–2334.

Rosenbluth, D., & Allman, J. M. (2002). The effect of gaze angle and fixation distance on the responses of neurons in V1, V2, and V4. *Neuron*, *33*(1), 143–149.

Salinas, E., & Sejnowski, T. J., (2001). Gain modulation in the central nervous system: where behavior, neurophysiology, and computation meet. The Neuroscientist: a review journal bringing neurobiology, neurology and psychiatry, 7(5), 430–440.

Sanchez, J. C., Carmena, J. M., Lebedev, M. A., Nicolelis, M. A., Harris, J. G., & Principe, J. C. (2004). Ascertaining the importance of neurons to develop better brain-machine interfaces. *IEEE transactions on bio-medical engineering*, *51*(6), 943–953.

Schwartz, A.B. (2004). Cortical neural prosthetics. Annu. Rev. Neurosci. 27, 487–507.

Seelke, A. M., Padberg, J. J., Disbrow, E., Purnell, S. M., Recanzone, G., & Krubitzer, L. (2012). Topographic Maps within Brodmann's Area 5 of macaque monkeys. Cerebral cortex (New York, N.Y. : 1991), 22(8), 1834–1850.

Sereno, M. I., & Huang, R. S. (2014). Multisensory maps in parietal cortex. Current opinion in neurobiology, 24(1), 39–46.

Sereno, M. I., & Huang, R. S. (2006). A human parietal face area contains aligned head-centered visual and tactile maps. Nature neuroscience, 9(10), 1337–1343.

Shipp, S., Blanton, M., & Zeki, S. (1998). A visuo-somatomotor pathway through superior parietal cortex in the macaque monkey: cortical connections of areas V6 and V6A. The European journal of neuroscience, 10(10), 3171–3193.

Snyder, L. H., Batista, A. P., & Andersen, R. A. (2000). Intention-related activity in the posterior parietal cortex: a review. Vision research, 40(10-12), 1433–1441.

Snyder, L. H., Batista, A. P., & Andersen, R. A. (1997). Coding of intention in the posterior parietal cortex. Nature, 386(6621), 167–170.

Sosulski, D. L., Bloom, M. L., Cutforth, T., Axel, R., & Datta, S. R. (2011). Distinct representations of olfactory information in different cortical centres. Nature, 472(7342), 213–216.

Spitmaan, M., Seo, H., Lee, D., & Soltani, A. (2020). Multiple timescales of neural dynamics and integration of task-relevant signals across cortex. PNAS, 117(36), 22522–22531.

Sussillo, D., & Abbott, L. F. (2009). Generating coherent patterns of activity from chaotic neural networks. Neuron, 63(4), 544–557.

Takahashi, K., Best, M.D., Huh, N., Brown, K.A., Tobaa, A.A., Hatsopoulos, N.G., (2017). Encoding of both reaching and grasping kinematics in dorsal and ventral premotor cortices. J. Neurosci. 37, 1733–1746.

Taoka, M., Toda, T., Iriki, A., Tanaka, M., & Iwamura, Y. (2000). Bilateral receptive field neurons in the hindlimb region of the postcentral somatosensory cortex in awake macaque monkeys. Experimental brain research, 134(2), 139–146.

Tosoni, A., Pitzalis, S., Committeri, G., Fattori, P., Galletti, C., & Galati, G. (2015). Resting-state connectivity and functional specialization in human medial parieto-occipital cortex. Brain structure & function, 220(6), 3307–3321

Triplett, M.A., & Goodhill, G.J., (2019). Probabilistic Encoding Models for Multivariate Neural Data. Front. Neural Circuits 13.

Truccolo, W., Hochberg, L.R., & Donoghue, J.P., (2010). Collective dynamics in human and monkey sensorimotor cortex: Predicting single neuron spikes. Nat. Neurosci. 13, 105–111.

Truccolo, W., Eden, U.T., Fellows, M.R., Donoghue, J.P., & Brown, E.N., (2005). A Point Process Framework for Relating Neural Spiking Activity to Spiking History, Neural Ensemble, and Extrinsic Covariate Effects. J. Neurophysiol. 93, 1074–1089.

Vaccari, F.E., Diomedi, S., Filippini, M., Galletti, C., & Fattori, P. (2021). A Poisson generalized linear model application to disentangle the effects of various parameters on neurophysiological discharges. STAR protocols, 2(2), 100413.

Vilarroya O. (2017). Neural Representation. A Survey-Based Analysis of the Notion. Frontiers in psychology, 8, 1458.

Walker, K. M., Bizley, J. K., King, A. J., & Schnupp, J. W. (2011). Multiplexed and robust representations of sound features in auditory cortex. The Journal of neuroscience: the official journal of the Society for Neuroscience, 31(41), 14565–14576.

Yuste R. (2011). Dendritic spines and distributed circuits. Neuron, 71(5), 772–781.

Zhang, C. Y., Aflalo, T., Revechkis, B., Rosario, E., Ouellette, D., Pouratian, N., & Andersen, R. A. (2020). Preservation of Partially Mixed Selectivity in Human Posterior Parietal Cortex across Changes in Task Context. eNeuro, 7(2), ENEURO.0222-19.2019.

Zhang, C.Y., Aflalo, T., Revechkis, B., Rosario, E.R., Ouellette, D., Pouratian, N., Andersen, R.A., (2017). Partially Mixed Selectivity in Human Posterior Parietal Association Cortex. Neuron 95, 697-708.e4.

Zipser, D., Andersen, R.A., (1988). A back-propagation programmed network that simulates response properties of a subset of posterior parietal neurons. Nature 331, 679–684.